REACTOR-BASED NEUTRINO OSCILLATION EXPERIMENTS

Giorgio Gratta
Physics Department, Stanford University, Stanford CA 94305-4060

ABSTRACT

We review the status of neutrino oscillation searches employing nuclear reactors as sources. This technique, a direct continuation of the experiments that proved the existence of neutrinos, is today an essential tool in investigating the indications of oscillations found in studying neutrinos produced in the sun and in the earth's atmosphere. The low energy of the reactor $\bar{\nu}_{\rm e}$ makes them an ideal tool to explore oscillations with small mass differences and relatively large mixing angles. In the last several years the determination of the reactor anti-neutrino flux and spectrum have reached a high degree of accuracy. Hence measurements of the $\bar{\nu}_{\rm e}$ flux at a given distance L can be readily compared with the expectation at $L = 0$, thus testing the disappearance. While two experiments with baselines of about 1 km, sensitive to the neutrino mass differences associated with the atmospheric neutrino anomaly, have collected data and published results in the last two years, an ambitious project with a baseline of more than 100 km is preparing to take data. This ultimate reactor experiment will have sensitivity sufficient to explore part of the oscillation phase space relevant to solar neutrino scenarios. It is the only envisioned experiment with a terrestrial source of neutrinos capable of addressing the solar neutrino puzzle.

© 2000 by Giorgio Gratta

Contents

1 Introduction **3**

2 Physics motivation of modern experiments **5**

2.1 Experimental indications for neutrino oscillations 5

2.2 Reactor versus accelerator-based oscillation experiments 8

3 Neutrino spectrum and flux determination **12**

3.1 Anti-neutrino production 13

3.2 Fission-rate estimates 14

3.3 From fission rates to $\bar{\nu}_{\mathrm{e}}$ and e^{+} spectra 17

3.4 Accuracy of the flux and spectrum predictions 18

4 Experiments motivated by the atmospheric neutrino anomaly **21**

4.1 Chooz 24

4.2 Palo Verde 25

4.3 Backgrounds 30

4.4 Results and systematics 36

4.5 Are smaller mixing angles within experimental reach ? 37

5 Exploring the solar ν anomaly on earth: KamLAND **41**

5.1 Nuclear reactors in Japan 41

5.2 Detector design 43

5.3 Expected performance 48

5.4 Other physics with a very large $\bar{\nu}_{\mathrm{e}}$ detector 49

6 Conclusions **52**

7 Acknowledgments **53**

1 Introduction

Neutrinos have the distinction of being the first elementary particles whose existence was predicted by a theorist in order to explain seemingly unrelated phenomena.[1] Pauli made such prediction in 1930 in his famous letter in order to explain the continuous electron energy distribution in nuclear beta decay. It became immediately clear that neutrinos will be difficult to observe, because the corresponding cross sections are so tiny. But in a series of experiments in 1953-56 Cowan, Reines and collaborators were able to prove convincingly that electron anti-neutrinos from nuclear reactors are able to cause the inverse neutron beta decay, $\bar{\nu}_{\rm e} + {\rm p} \to {\rm e}^+ + {\rm n}$, and hence that they are real particles. Shortly afterwards, in 1962, the separate identity of the muon neutrinos, ν_μ, was demonstrated. Another decade later, in 1975, the tau lepton was discovered and the observation of its decay properties implied the existence of the third neutrino, ν_τ, which was directly observed only in the last year.[2] Precise measurements of the decay width of the Z have shown that just three neutrino flavors participate in the weak interactions (at least for neutrinos with masses less than $1/2\, M_{\rm Z}$).

Ironically, while our knowledge of intrinsic neutrino properties remains quite poor, these particles have been used as tools to understand other phenomena. The tradition of underground detectors began thirty years ago when Davis and his collaborators were first able to detect neutrinos from the Sun. This was, and still is, the only clear proof that the basic energy generation in stars is understood. The birth of neutrino astronomy can be associated with the observation of the neutrino burst from the supernova 1987A. Neutrino-induced reactions played an important role in establishing what is now known as the Standard Model of electroweak interactions when in 1973 the neutral currents were discovered via the observation of the $\nu_\mu + e \to \nu_\mu + e$ scattering as well as the neutral current scattering of neutrinos on nucleons. Finally, neutrinos have been extensively used in deep inelastic scattering experiments at CERN and FNAL, exploring the quark structure of nucleons.

The main problem in neutrino physics today is the question whether neutrinos, like the charged fermions, have a mass.[3,4] The experimental hints for neutrino mass are at present based on the phenomenon of neutrino oscillations. If neutrinos are massive particles which behave in analogy to quarks, the states with a definite mass (i.e., the "mass eigenstates" which propagate as plane waves in a vacuum) are not necessarily the partners of the charged leptons that couple to the vector bosons $\rm W^\pm$ in doublets

(i.e., the weak eigenstates)

$$\left(\begin{array}{c} \nu_{\rm e} \\ {\rm e}^- \end{array} \right) , \left(\begin{array}{c} \nu_\mu \\ \mu^- \end{array} \right) , \left(\begin{array}{c} \nu_\tau \\ \tau^- \end{array} \right) . \tag{1}$$

The weak eigenstates $|\nu_l\rangle$ will be in such a case linear superpositions of the mass eigenstates $|\nu_i\rangle$

$$|\nu_l\rangle = \sum_i U_{l,i} |\nu_i\rangle \ , \tag{2}$$

where the coefficients $U_{l,i}$ form the leptonic mixing matrix. If we assume that only three neutrinos can contribute in the Eq. (2) above, then U is a unitary 3×3 matrix.

If Eq. (2) is valid, we encounter the phenomenon of neutrino oscillations in which a neutrino which was initially in the weak eigenstate l can be spontaneously transformed, at least in part, into another weak eigenstate neutrino of flavor l'. To see how that happens, consider the time development of the mass eigenstate $|\nu_i\rangle$

$$|\nu_i(t)\rangle = e^{-i(E_i t - p_i L)} |\nu_i(0)\rangle \simeq e^{-i(m_i^2/2E)L} |\nu_i(0)\rangle \ , \tag{3}$$

where L is the flight path and in the last expression we assumed that the laboratory momenta and energies are much larger than the neutrino rest masses m_i. Let us consider now the propagation of a neutrino which was created at $L = 0$ as a weak eigenstate $|\nu_l\rangle$. At a distance L this state is described by

$$|\nu_l(L)\rangle \simeq \sum_i U_{l,i} e^{-i(m_i^2/2E)L} |\nu_i\rangle \ \simeq \ \sum_{l'} \sum_i U_{l,i} e^{-i(m_i^2/2E)L} U^*_{l',i} |\nu_{l'}\rangle \ . \tag{4}$$

Thus, the neutrino of flavor l acquired components corresponding to other flavors l'. This is a purely quantum mechanical effect, a consequence of the coherence in the superposition of states in Eq. (2). The probability that the "transition" $l \to l'$ happens at L is obviously

$$P(\nu_l \to \nu_{l'}, L) = |\sum_i U_{l,i} U^*_{l',i} e^{-i(m_i^2/2E)L}|^2 \ . \tag{5}$$

This is an oscillating function of the distance L. The oscillation length depends on the neutrino masses m_i (actually on the differences of mass squares), and the oscillation amplitude depends on the mixing matrix U.

Neutrino oscillation experiments are often analyzed in a simplified way by assuming that only two neutrino flavors mix, e.g. e and μ. The mixing matrix U then depends only on one mixing angle θ, and the oscillation probability, Eq. (5), is also simplified,

$$U = \left(\begin{array}{cc} \cos\theta & \sin\theta \\ -\sin\theta & \cos\theta \end{array} \right) \ , \ P(\nu_{\rm e} \to \nu_\mu, L) = \sin^2 2\theta \sin^2(\Delta m^2 L/4E) \ . \tag{6}$$

Here $\Delta m^2 \equiv m_1^2 - m_2^2$. The probability that $\nu_{\rm e}$ remains $\nu_{\rm e}$ is obviously $P(\nu_{\rm e} \to \nu_{\rm e}, L) = 1 - P(\nu_{\rm e} \to \nu_\mu, L)$.

In this two-flavor scenario the oscillation amplitude is $\sin^2 2\theta$ which vanishes if $\theta = 0$ or 90° and is maximum if θ =45°. The oscillation length is

$$L_{osc} = 2\pi \frac{2E_\nu}{\Delta m^2} = \frac{2.48 E_\nu({\rm MeV})}{\Delta m^2({\rm eV}^2)} {\rm meters}\ . \tag{7}$$

To test for oscillations, one can perform either an *appearance* search in which one looks for new neutrino flavor, or a *disappearance* test in which one looks for a change in the flux normalization. In either case, tests performed at distance L are only sensitive to the values of Δm^2 for which $L \geq O(L_{osc})$.

So far we have considered only propagation of neutrinos in a vacuum. When neutrinos propagate in matter, such as in the solar interior, the oscillation pattern may be modified. This happens because electron neutrinos can forward scatter on electrons by charged current interactions, and other neutrino flavors cannot. Under favorable circumstances a resonance enhancement of the oscillation amplitude, the so-called Mikheyev-Smirnov-Wolfenstein (MSW) effect,[5] can take place.

2 Physics motivation of modern experiments

Numerous searches for neutrino oscillations were performed during the last two decades using nuclear reactors as well as particle accelerators as sources. Most of them resulted in an "exclusion plot", i.e., based on them certain ranges of the parameters Δm^2 and $\sin^2 2\theta$ can be excluded from further considerations as shown in Figure 1. However, at the present time there are three groups of measurements that suggest the existence of neutrino oscillations. (And, at the same time, the parameter ranges suggested by them are not excluded.) Only these *positive* results will be briefly discussed here (other experiments are listed in the Review of Particle Properties[6]).

2.1 Experimental indications for neutrino oscillations

The most prominent group of measurements which are commonly interpreted as evidence for neutrino oscillations are usually referred to as the "atmospheric neutrino anomaly".[7] Primary cosmic rays impinging on the nitrogen and oxygen nuclei at the top of the earth's atmosphere produce mostly pions, which subsequently decay via the chain $\pi \to \mu \bar{\nu}_\mu, \mu \to {\rm e} \bar{\nu}_{\rm e} \nu_\mu$. At sufficiently low energy, when such a chain can

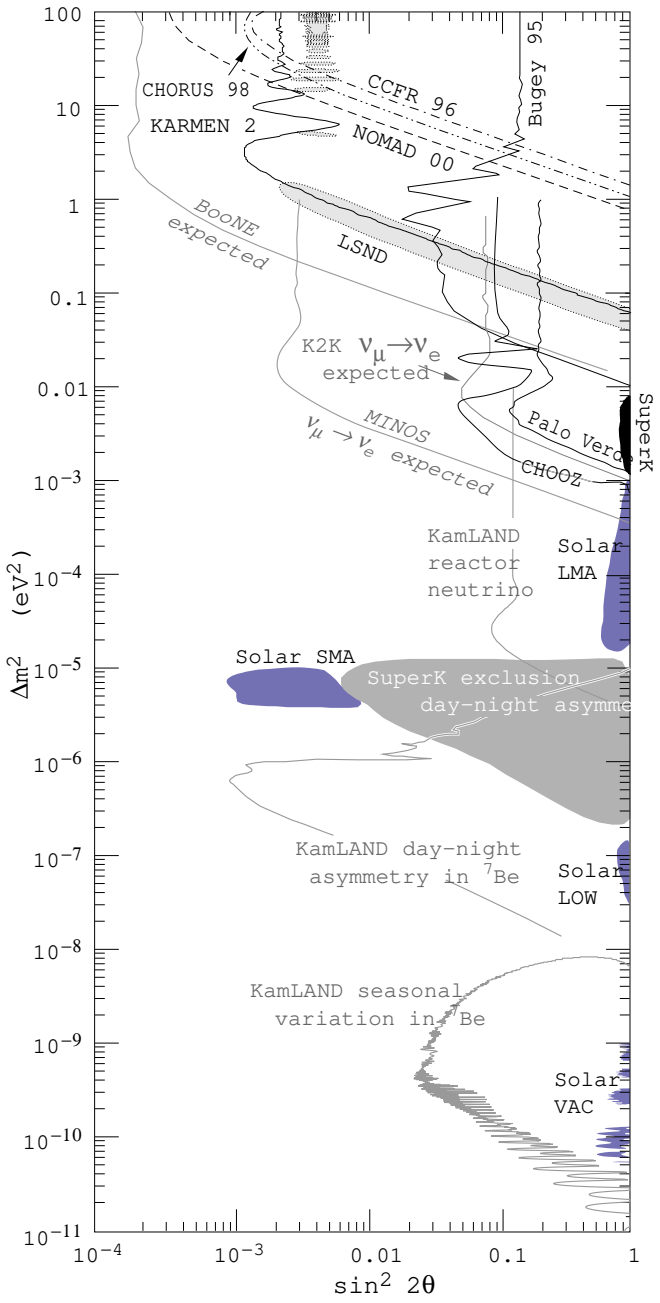

Fig. 1. Phase-space for neutrino oscillations. The existing limits on $\nu_e - \nu_\mu$ are compared with current and future experiments and the regions obtained by interpreting the solar, atmospheric and LSND neutrino anomalies as due to oscillations (note that some of these three effects are not necessarily to be regarded as oscillations of the $\nu_e - \nu_\mu$ type). The MSW mechanism is used in plotting some of the solar neutrino regions. The sensitivity of reactor experiments is the same for $\nu_e - \nu_\tau$ oscillations. Limits are at 90% CL. The two bottom KamLAND sensitivity curves refer to direct solar neutrino observations that are not discussed in this paper.

fully develop, the resulting atmospheric neutrinos therefore are expected to follow the $\nu_\mu : \nu_{\rm e} = 2 : 1$ ratio, which is essentially independent of the details of the complicated process that created them. In addition, in an underground detector, one can deduce the direction of the incoming neutrinos from the direction of the leptons (e and μ) created by the charged current interactions. Again, one is reasonably confident that this zenith angle distribution can be accurately predicted. If the ν_μ and/or $\nu_{\rm e}$ neutrinos oscillate, one expects deviations from the 2:1 ratio mentioned above. Also, since the zenith angle is simply related to the neutrino path length, one expects deviations from the expected zenith angle dependence of the lepton yield.

Both signatures of neutrino oscillations were in fact observed. The ν_μ/ν_e ratio is noticeably smaller, only about 60%, than the expected value. This result has been confirmed in four detectors thus far. The anomalous zenith angle dependence was first observed in Kamiokande, and has been now confirmed, with much better statistical significance, by SuperKamiokande. If these effects indeed signify neutrino oscillations (and we do not have another viable explanation) then the corresponding mixing angle is large, $\sin^2 2\theta \approx 1$. The value of the mass parameter Δm^2 remains uncertain, but is clearly in the range 10^{-2} - 10^{-4} eV^2.

The second set of measurements that can be interpreted as evidence for neutrino oscillations deals with the "missing" solar neutrinos.[8] The Sun produces an intense flux of electron neutrinos as a byproduct of the fusion reactions which generate solar power. It is believed that the solar structure is understood sufficiently well so that the flux and energy spectrum of the solar neutrinos can be confidently predicted. The solar neutrino fluxes have been measured in five experiments so far. All of them report a deficit, i.e., the measured flux is less than the expected one. Moreover, the reduction depends on the neutrino energy, inferred experimentally from the thresholds of the individual detectors. The only viable explanation of the deficit appears to be neutrino oscillation (ν_e disappearance). By contrast to the attempts to explain the deficit by modification of the solar model, which are unsuccessful, all existing data can be simply and elegantly explained by invoking neutrino mass. In particular, the solution based on the MSW effect offers the most popular scenario. Treating the problem in the two-flavor framework explained above, one arrives at two isolated islands in the Δm^2 – $\sin^2 2\theta$ plane. Both solutions correspond to $\Delta m^2 \approx 10^{-5}$ eV^2. One of them has rather small $\sin^2 2\theta \approx 10^{-2}$. The other one has much larger mixing angle, $\sin^2 2\theta \geq 0.5$. This solution also spans a larger interval of Δm^2 extending up to 10^{-4} eV^2.

Finally, the only indication for oscillations involving man-made neutrinos comes

from the LSND experiment which finds evidence for the $\bar{\nu}_\mu \rightarrow \bar{\nu}_\mathrm{e}$ and, with more limited statistics, also for $\nu_\mu \rightarrow \nu_\mathrm{e}$.[9] The former channel uses neutrinos from the pion and muon decay at rest, with energies less than $m_\mu/2$. The latter channel uses neutrinos from the pion decay in flight which have somewhat higher energies. These are appearance experiments; the observed signal should be absent if neutrinos do not oscillate. The well determined quantity is the oscillation probability, which has the value of about 3×10^{-3}. This result has not been independently confirmed but it is not contradicted by other evidence either.

As we can see from this brief discussion, the last decade brought us a number of clues. With the exception of the LSND signal, they all came from measurements involving neutrinos produced by natural sources outside of our control. A number of new experiments has been performed or is in various stages of planning in order to investigate further these tantalizing effects. Reactor experiments play an all-important role in this quest, owing to their unique ability to investigate very small neutrino-mass differences.

Like in many other aspects of neutrino physics there is a fundamental difference between the past reactor oscillation experiments[10–13] and the more recent experiments with baselines of 1 km or more: experiments in this last category are designed to further investigate in a controlled environment, with man-made neutrinos, particular regions of the oscillation parameter space where we do have indications for oscillation from other experiments. Hence the results from this new generation of detectors directly impact our understanding of the neutrino mixing matrix.

2.2 Reactor versus accelerator-based oscillation experiments

Nuclear reactors produce isotropically $\bar{\nu}_\mathrm{e}$ in the β decay of the neutron-rich fission fragments. All detectors optimized for oscillation searches take advantage of the relatively large cross-section and specific signature of the inverse-β-decay reaction $\mathrm{p} + \bar{\nu}_\mathrm{e} \rightarrow \mathrm{n} + \mathrm{e}^+$. This cross-section is shown in Figure 2 as a function of the neutrino energy along with the the neutrino flux at the reactor and the resulting interaction rate in a detector. We note here that the detection reaction has a threshold of about 1.8 MeV, as will be discussed in more detail later. Many of the merits and limitations of reactor-based experiments can be understood observing that the energy of $\bar{\nu}_\mathrm{e}$ is rather low, in the few-MeV range. It directly follows that reactor-based experiments can only be of $\bar{\nu}_\mathrm{e}$-disappearance type since the neutrino "beam" does not have sufficient energy to

produce muons (or τs !) and the neutral-current reaction of an "oscillated" $\bar{\nu}_\mu$ or $\bar{\nu}_\tau$ on electrons has too low a cross-section and is indistinguishable from the many backgrounds present. This first limitation makes reactor-based experiments well suited only for investigating relatively large mixing parameters. In practice experiments have reported mixing sensitivities around 10% at large Δm^2 (although the proposal for a very ambitious experiment with sensitivity better than 2% at a particular Δm^2 will be discussed later). The second limitation of reactor-based oscillation searches derives from

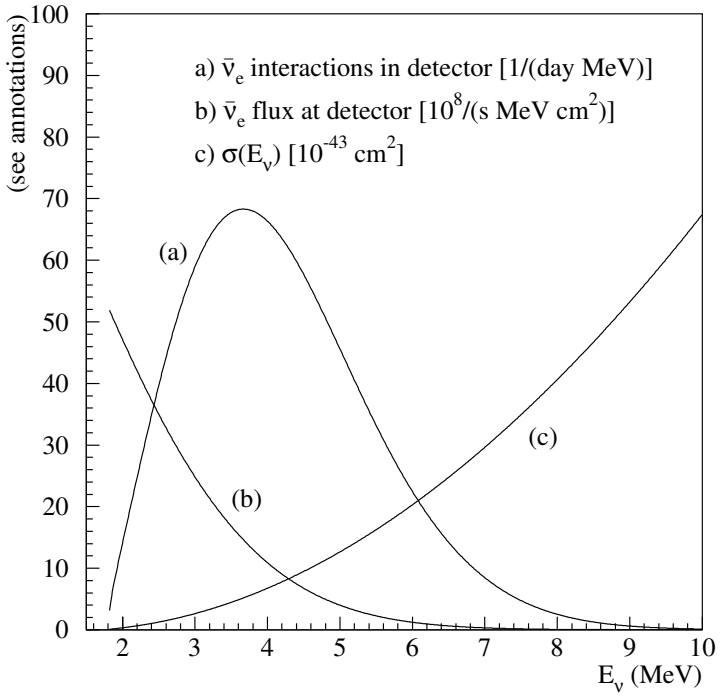

Fig. 2. $\bar{\nu}_e$ flux, inverse beta decay cross section, and $\bar{\nu}_e$ interaction spectrum at the detector.

the fact that the only known method of collimating neutrino beams employs the Lorentz boost of the parent particles from which decay the neutrinos are produced. For this reason low energy neutrinos are generally produced over large solid angles while high energy ones may come in relatively narrow beams. Obviously a reactor emits $\bar{\nu}_\mu$ in a completely isotropic way, and this, together with the modest interaction cross-sections available at low energy, make the specific signal rather low. At the same time, however, the low energy neutrinos provide us with a unique opportunity to probe the lowest regions of Δm^2 that are otherwise beyond the reach of accelerator-based searches. Some

of these tradeoffs are well illustrated by Figure 3 where the Δm^2 sensitivity is shown, together with the necessary baseline, versus the reactor power and detector fiducial mass for different statistical accuracies.

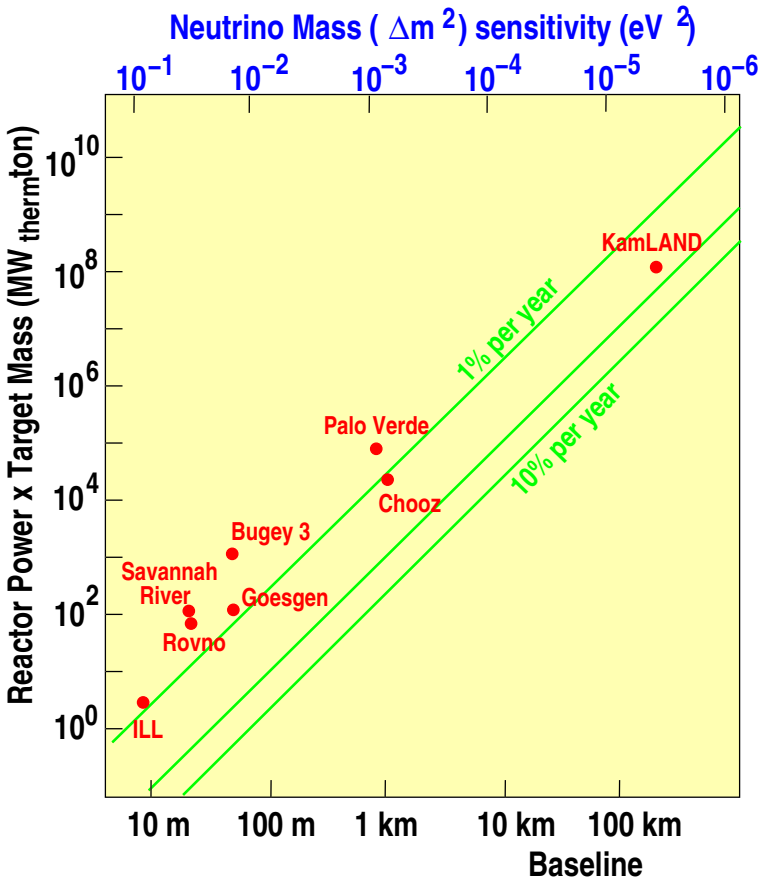

Fig. 3. Neutrino Δm^2 sensitivity as a function of total reactor power and detector fiducial mass for detection based on the inverse-β reaction discussed in the text. The baseline scales with the Δm^2 sensitivity sought, according to Eq. 7. The fiducial-mass$\times$power necessary for the experiment grows with the square of the baseline.

Oscillation searches using reactors as sources are particularly important today since several of the indications for neutrino oscillations shown in Figure 1 point to regions of the parameter space at very small Δm^2 and nearly-full mixing. Hence two reactor-based experiments were performed to investigate the phenomenon of atmospheric neutrinos as $\bar{\nu}_{\rm e} - \bar{\nu}_{\rm X}$-oscillations. Such experiments, described in detail below, had baselines of about 1 km and fiducial masses of the order of 10 tons. In comparison the

accelerator-based Minos project between FNAL and the Soudan mine[9] will access similar Δm^2 values with GeV-energy neutrinos and a baseline of the order of 1000 km. However the 5.4 kton Minos detector will be able to investigate also oscillation channels not including $\bar{\nu}_{\rm e}$ and reach a mixing parameter sensitivity substantially better than 1%.

The reactor-based KamLAND experiment, with a baseline larger than 100 km, will offer the unique opportunity of testing, with man-made neutrinos, the large-mixing-angle MSW solution of the solar neutrino puzzle. In this case the restriction to $\bar{\nu}_{\rm e} - \bar{\nu}_{\rm X}$-oscillations does not limit the interest of the experiment (since solar neutrinos do certainly involve $\nu_{\rm e}$!), while its Δm^2 sensitivity is well beyond what can be practically achieved by accelerators. (For comparison, similar Δm^2 sensitivity could be achieved in an accelerator-based experiment with baselines of order 10^5 km, larger than the diameter of the earth.)

Of course the relatively lower energy of neutrinos from reactors pushes the optimization of reactor-based experiments to concentrate on the reduction and rejection of backgrounds from natural radioactivity that is, on the other hand, hardly an issue in accelerator-based detectors. In this respect the correlated signature from the inverse-β process described plays a very important role, as will be described in detail later.

While in the case of neutrinos produced by accelerators the experimenter has full control over the status of the beam, the flux of $\bar{\nu}_{\rm e}$ cannot be changed at will in commercial power nuclear reactors. However, in practice, typical reactor optimization requires a refueling shutdown every 12 to 24 months. Such shutdowns usually last about a month, providing a rather convenient flux modulation that can be used to validate background subtraction methods. As explained in detail later, even in the case of KamLAND, which observes the neutrinos from about 70 reactor cores, a substantial flux modulation is provided by the coincidence of scheduled refueling outages in the Spring and Fall periods, when electricity demand is lowest.

Finally we remark here that the fully isotropic flux produced by nuclear reactors eliminates the problems related with beam pointing that are present in experiments using accelerators. While the pointing accuracy required in these experiments is well within the present technology, a fool-proof cross check of the beam-detector alignment is certainly not trivial to obtain.

In conclusion, reactor-based and accelerator-based experiments offer complementary approaches to the quest for neutrino oscillations. It is likely that only the combined efforts on these two fronts, together with other studies such as the search for

neutrino-less double-β decay, will allow us to elucidate the problem of mixing in the lepton sector.

3 Neutrino spectrum and flux determination

Since reactor-based oscillation experiments are of the disappearance type, the accurate determination of the $\bar{\nu}_{\rm e}$ spectrum and absolute normalization at the reactors is an essential ingredient of the measurements. We note here that for oscillation parameters well within the experiment's sensitivity the evidence for oscillations would manifest itself as a deficit of events accompanied by a distortion of the energy spectrum, as shown by the example[14] in Figure 4. However, as the true value of the oscillation parameters moves closer to the sensitivity boundary of the experiment, the spectral shape loses power and the accuracy of the measurements essentially relies on the total event count and, hence, the knowledge of the absolute reactor flux. This last scenario also corresponds to the more usual case in which no oscillations are observed and an upper limit is set.

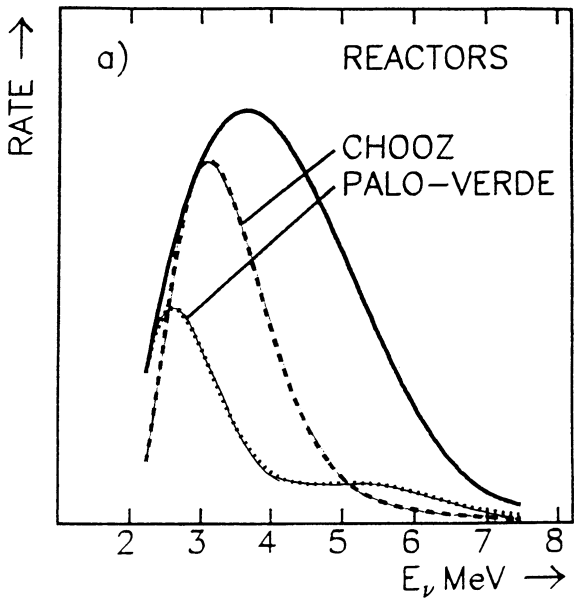

Fig. 4. Expected energy spectra[14] for no oscillations and oscillations with parameters $\Delta m^2 = 7.2 \times 10^{-3}$ eV^2 and $\sin^2 2\theta = 1$ at the Chooz ($L \simeq 1$ km) and Palo Verde ($L \simeq 0.8$ km) experiments.

While in this section we will concern ourselves mainly with *a priori* reactor $\bar{\nu}_{\rm e}$ yield determinations, multiple-baseline measurements are possible and have been performed

in the past at the Goesgen[11] and Bugey[12,13] reactors. Indeed such measurements helped in gaining confidence in the reactor yield estimates, and, although they were not attempted by Palo Verde and Chooz, they have been recently proposed for a more accurate determination of the mixing angle θ_{13} for the atmospheric neutrino region $\Delta m^2 \approx 10^{-3}$ eV^2.[15]

We note that, while the methods described here are very general, most of the details discussed in this section specifically derive from the Palo Verde experiment.[16]

3.1 Anti-neutrino production

The estimate of the $\bar{\nu}_{\rm e}$ yield proceeds, schematically, in three steps. First the thermal power of each reactor core is measured, generally daily, so that, starting from the initial fuel composition, the burn-up state can be computed as function of time. Small corrections due to other reactor parameters that modify the criticality of the core are also introduced at this time. Reactor simulation codes are often used at this stage and produce an accurate instantaneous fission rate throughout the fuel cycle. In a second step the neutrino spectrum is derived from the fission rate. Generally both data from direct β^- measurements for three of the dominant fissile isotopes and theoretical estimates are used. These two approaches give consistent results. In the final step an experimental e^+ spectrum in the detector is derived and compared with data.

It should be stressed that a good over-all cross check of this procedure is provided by the inspection of older (shorter baseline) experiments. The coincidence of their measured spectrum with the prediction based on the procedure described above can be interpreted as if the older experiments were, as far as many of the errors are concerned, near detectors in a two baseline measurement. This is so because, unlike for the case of accelerator-produced neutrinos, most commercial reactors are remarkably similar to each other in terms of neutrino production and there are no beam focusing or steering effects. All this notwithstanding, there are certain advantages in real two-baseline measurements, as will be discussed in a later section.

It is useful here to mention that typical modern commercial Light Water Reactors (LWR) have thermal powers of the order of 3 GW$_{th}$. This figure applies to both Pressurized Water Reactors (PWR) and to the less common Boiling Water Reactor (BWR) designs. In both cases the fuel is enriched to $2-5\%$ ^{235}U. Since on average a fission produces $\sim$ 200 MeV and ~ 6 $\bar{\nu}_{\rm e}$ we conclude that the typical yield is $\sim 6 \times 10^{20}$ $\bar{\nu}_{\rm e}$ core^{-1} s^{-1} (of course part of this flux will be below the detection

threshold, see Figure 2).

The existence of a 1.8 MeV threshold in the detection process $\bar{\nu}_{\rm e} + {\rm p} \rightarrow {\rm n} + {\rm e}^{+}$ insures that the observed $\bar{\nu}_{\rm e}$ signal tracks very closely in time the power excursions in the reactor. In fact only $\bar{\nu}_{\rm e}$ from large Q-value, and hence short half-life, β-decays are detected. This is of some practical importance as large quantities of spent fuel are usually stored on-site by reactor operators. There is no need to track the inventory of spent fuel and, in fact, after a few hours from reactor turn on/off the $\bar{\nu}_{\rm e}$ flux can be considered to be at regime.

3.2 Fission-rate estimates

The four isotopes whose fission and decay chains are the source of virtually all the power and neutrino yields are ^{235}U, ^{238}U, ^{239}Pu, and ^{241}Pu. The fission rates deriving from their evolution during a typical fuel cycle in one of the Palo Verde reactors is shown in Figure 5 as calculated by a core simulation program.[16] For comparison we also show the evolution of ^{240}Pu and ^{242}Pu which give the next-to-leading contributions. The contribution of these isotopes is of order 0.1% or less and will not be considered further.

Each isotope produces a unique neutrino spectrum through its decay chain, so plutonium breeding results in a significant change in the emitted neutrino spectrum.

Two types of errors can be attributed to the isotope compositions described in Figure 5: errors deriving from uncertainties in the initial fuel composition and in the measurement of the plant parameters that are used as input to the simulation, and errors due to imperfect core and neutronics modeling by the simulation program itself. The errors intrinsic to the simulation are known to contribute substantially less than 1% to the neutrino yield uncertainty, from tests in which fuel is sampled and analyzed for isotopic composition at the end of a fuel cycle. The results usually agree well with the predictions from the cycle simulation.

The correlation between the $\bar{\nu}_{\rm e}$ yield and the plant parameters used as input to the simulation is shown in Figure 6. Apart from the obvious correlation with the thermal power, other parameters enter the simulation because they affect the criticality by altering the neutron transport in the core (generally by the water density and boron absorber concentration). In general we see that for the parameter with largest correlation besides power, the cold legs water temperature ("T inlet"), an error of 10% produces an uncertainty of only 0.15% in the $\bar{\nu}_{\rm e}$ yield. Of course the inlet temperature is known to much

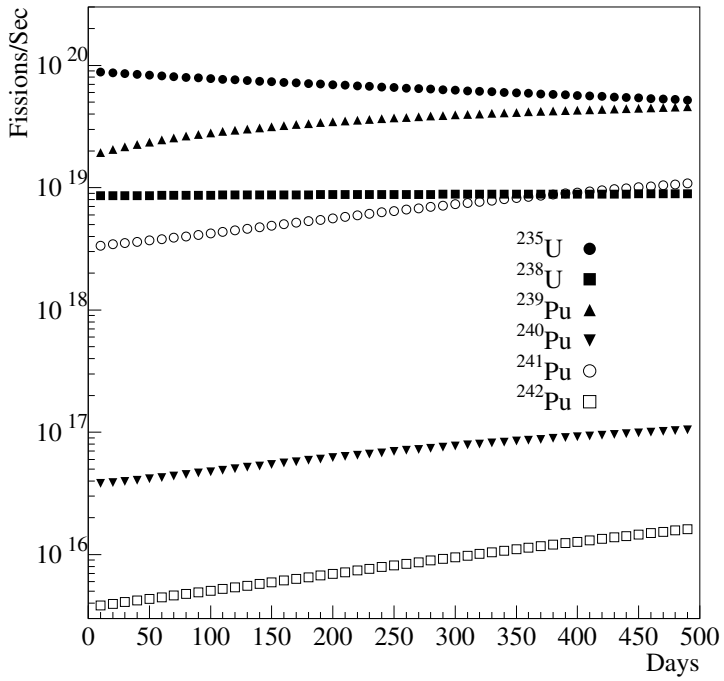

Fig. 5. Time evolution of fission rates for each of the six most important isotopes in one of the Palo Verde reactor cores. The horizontal scale covers a full fuel cycle, at the end of which about 1/3 of the core is replaced with fresh fuel. Only the four most important isotopes are normally used to predict $\bar{\nu}_e$ yields.

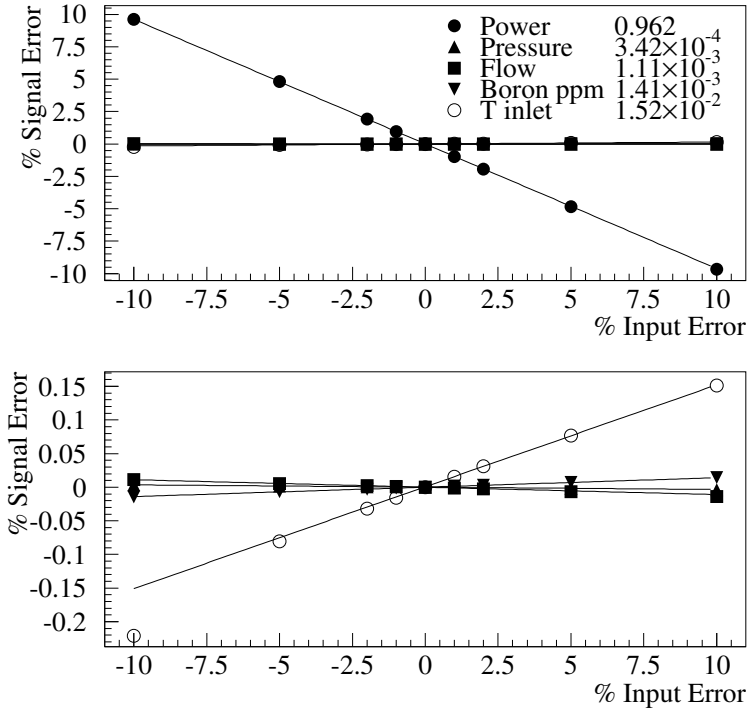

Fig. 6. Correlation between $\bar{\nu}_e$ yield and the five most important inputs to the core simulation for a PWR. The numbers in the key are the slopes of the fitted lines. Note that a variation of even 10% in any of the parameters, except power, has little effect on the output of the simulation.

better than 10%.

Economic reasons and safety provide plant operators with an incentive to accurately measure the thermal power of the reactors. Indeed, usually more than one method is used and the results are compared to understand the size of the uncertainties. Generally calorimetric methods (simultaneous measurement of temperature and flow-rate of the water outlet in the secondary cooling loop) give the smallest error (0.7% at Palo Verde) and are used as the primary power estimate.

3.3 From fission rates to $\bar{\nu}_e$ and e^+ spectra

The instantaneous fission rates of the four isotopes ^{235}U, ^{238}U, ^{239}Pu, and ^{241}Pu found above are then converted into a $\bar{\nu}_e$ spectrum. For all but ^{238}U direct measurements of the beta spectrum from fissioning by thermal neutrons exist.[17,18] These are converted to neutrino spectra by fitting the observed β spectra to a set of 30 hypothetical β-branches. However, Refs.[17,18] do not include ^{238}U fission, which requires faster neutrons than were available for those measurements. While this is unfortunate and a measurement

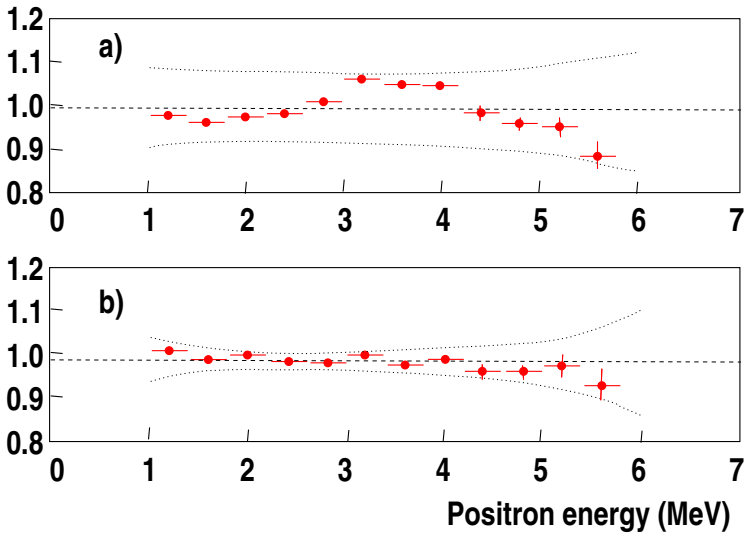

Fig. 7. Ratio between Bugey 3 measurements and different predictions.[13] In a) the measurements are compared to *a priori* calculations.[20] In b) Bugey 3 data is compared to the prediction obtained using β spectra measurements[17,18] (and the calculation mentioned for ^{238}U). The dashed envelopes are estimates of the overall systematics.

would certainly be welcome, the lack of data is of no major practical consequence

since ^{238}U only contributes $\sim 8\%$ to the total power and $\sim 11\%$ to the neutrino signal. *A priori* theoretical calculations of the β spectrum have been performed[19,20] for each of the four isotopes discussed here. These calculations typically consider the decays of ~ 750 isotopes, of which ~ 250 have measured β spectra. As shown in Figure 7 a), a rather good agreement was found between the calculated spectra and the ones measured, as described above, for ^{239}Pu, ^{241}Pu and ^{235}U. In terms of integrated flux above threshold the agreement is certainly better than 10%. Hence it is assumed that using the calculation for ^{238}U should produce an additional error of the order of better than 1%.

Finally the neutrino spectrum emitted by the reactors must be converted into an estimate of the experimental observable, the positron spectrum in the detector. Assuming no oscillations, there are three contributions to this calculation: the distance to each core, the cross section for $\mathrm{p} + \bar{\nu}_\mathrm{e} \longrightarrow \mathrm{n} + \mathrm{e}^+$, and the number of target protons.

The distance to the reactors is of course trivially obtained with negligible uncertainty. The cross section for inverse-β decay has been calculated[21] and also the angular distribution.[22] The lowest order cross section was modified for several effects such as neutron recoil, weak magnetism, and radiative corrections. The estimated accuracy of the resulting modified cross section is about 1%.

The number of protons in the target requires knowledge of the chemical composition and mass of both scintillator and possible other detector materials where $\bar{\nu}_\mathrm{e}$ can be captured and recorded with finite efficiency. Typically errors smaller than 1% are achievable for this parameter.

3.4 Accuracy of the flux and spectrum predictions

The ultimate check of the accuracy of the prediction outlined above consists of comparing the results, in terms of the $\bar{\nu}_\mathrm{e}$ energy spectrum, with the measurements performed in short baseline reactor oscillation experiments. Since such experiments have not reported the observation of oscillations we can assume that their measurements represent the direct observation of the reactor spectrum at production. This statement is reinforced by the fact that some of the short baseline experiments such as Gösgen[11] or Bugey[12,13] did measurements at different baselines, observing no difference between the spectra. This is shown for Gösgen in Figure 8. In particular the relatively recent Bugey 3 measurements were performed at 15-40 m distance from the core and recorded very high statistics (some 1.5×10^5 $\bar{\nu}_\mathrm{e}$ events). The good agreement between Bugey 3

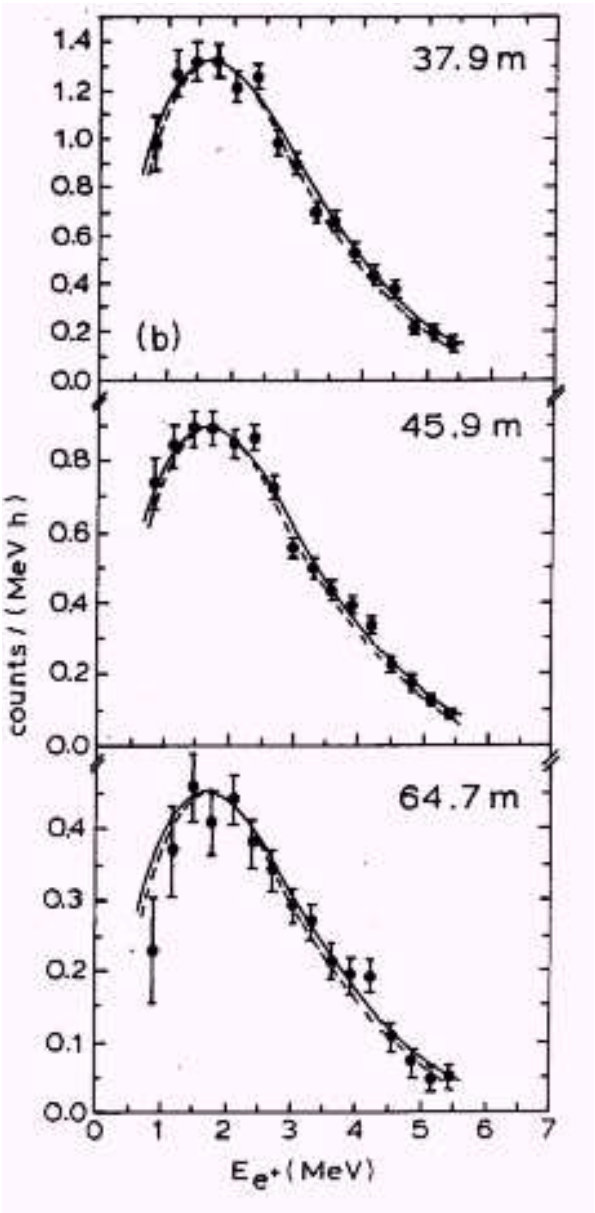

Fig. 8. Positron spectrum observed by the Gösgen experiment for three different baselines. The continuous lines represent fits to the predictions obtained, as described in the text, using ILL data and theoretical calculations.

data and the non-oscillation predictions is shown in Figure 7. In panel a) the prediction is generated purely from theory. Of more practical importance is panel b) where the prediction derives from β spectra (except for ^{238}U where theory is used). In this case a fit to an horizontal line gives a level of 0.99 with $\chi^2/d.o.f. = 9.2/11$. The final Bugey 3 result is quoted as having a 1.4% total uncertainty.

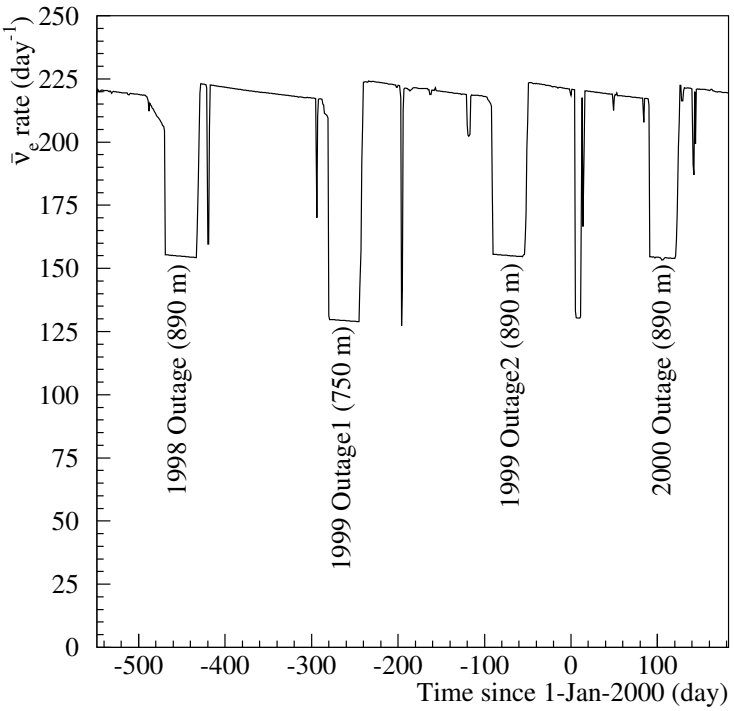

Fig. 9. Expected number of $\bar{\nu}_e$ interactions in the Palo Verde detector during the $\sim$2 years of data-taking of the experiment. The history displayed is rather typical for a multi-core power plant with regular refueling periods (about 1 month-long each) and unscheduled reactor trips. Note that one reactor is closer to the experiment while the other two are equidistant, this explains the different excursion for one of the refuelings. The steady decline in $\bar{\nu}_e$ interactions during the cycle is the effect of fuel burn-up.

For reference we give in Figure 9 the time evolution of the $\bar{\nu}_e$ interaction rate expected in the Palo Verde detector, calculated as described above from the plant data. The time evolution is typical of a plant with more than one reactor. Refueling outages (about 1 month long each) have different amplitudes because of the different distances between the reactors and the detector. Short accidental reactor trips are also visible along with the steady rate decline through the reactor cycle due to fuel burn-up.

4 Experiments motivated by the atmospheric neutrino anomaly

Two experiments have been built with the specific purpose of testing the hypothesis that neutrino oscillations occur with the parameters found by the atmospheric neutrino measurements. While Chooz is completed and all their data is published,[23,24] data-taking at Palo Verde finished in the summer 2000 and results from the first half of the data-set are published.[25,26] Palo Verde data presented here refers to this first half of the data-set, while the analysis of the second half should be published soon.

As can be seen from Figure 3, in order to access $\Delta m^2 \approx 10^{-3}$ eV^2 with reactor neutrinos, a baseline of order 1 km and a mass in excess of a few tons are needed. Indeed the backgrounds from cosmic radiation and natural radioactivity are a major consideration in the design of such large, low-energy detectors, and different background situations led the two groups to rather different designs.

The Chooz detector was built in a pre-existing underground cavity under a $\simeq 100$ m rock overburden ($\simeq 300$ m.w.e). This substantial cosmic radiation shielding allowed the use of a homogeneous detector where inverse-β events were tagged as a double (delayed) coincidence between the e^+ (prompt) signal and the n (delayed) one. In turn this simple event signature can be identified with large efficiency, so that a 5 ton active mass was sufficient for the experiment. The Palo Verde detector, on the other hand, was located in an underground bunker excavated for the purpose. Economic considerations limited the overburden to 12 m ($\simeq 32$ m.w.e.) sufficient only to eliminate the hadronic component of the cosmic radiation and reduce the muon flux by a factor of five. The rather large remaining muon flux produced a substantial quantity of secondary neutrons, so that a segmented detector was needed to take full advantage of the triple coincidence given by the e^+ ionization and subsequent γ's from annihilation. This more elaborate topological signature reduced the detector efficiency and pushed the fiducial mass to 12 ton. Both detectors were built with materials selected for low radioactivity and included a passive γ and neutron shield and an active cosmic-ray veto counter.

While the 3-reactor plant of Palo Verde produces a larger power (11.6 $GW_{\rm ther}$) than the 2-reactor one at Chooz (8.5 $GW_{\rm ther}$), more important is the fact that, unlike in the case of Palo Verde which was a plant running at regime, the Chooz reactors were commissioned after the start of data taking at the experiment. This endowed the collaboration with the rather unique opportunity of observing the backgrounds at reactor-off for a substantial period and the slow ramp-up of power. On the other hand

the need to cope with a much more stable operation, with the periodic $\sim 2/3$ refueling power excursions shown in Figure 9, motivated the Palo Verde group to develop new methods for background subtraction that will be important for future experiments that will be likely to run in similar steady-state situations.

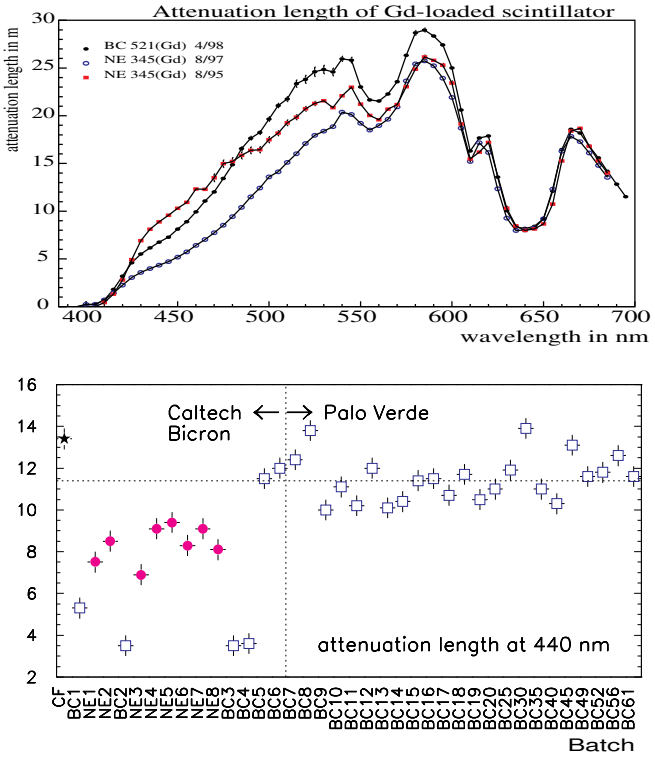

Fig. 10. Initial light attenuation length in Palo Verde scintillator. Top: attenuation length as function of wavelength in three scintillator batches. Bottom: attenuation length at $\lambda = 440$ nm for the initial batches of scintillator. Production batches are to the right of the vertical dashed line, while on the left we show various test batches not used in the detector. The first point ("CF") refers to a standard (non Gd loaded) scintillator fluid. Typical production scintillator had an attenuation length better than 11 m.

Both detectors used liquid scintillator loaded with 0.1% natural gadolinium, which has a high thermal neutron capture cross-section and releases a large amount of energy in the capture. In this way the neutron capture time is reduced to $\sim$27 μs from $\sim$170 μs for the unloaded scintillator, proportionally reducing the uncorrelated background. Furthermore, Gd de-excitation after the capture releases a 8 MeV γ cascade, whose summed energy gives a robust event tag well above natural radioactivity. In contrast, neutron capture on protons releases only a single 2.2 MeV γ. While the Gd loading offers obvious advantages in suppressing backgrounds, it is not easy to achieve

in the stable and sufficiently transparent form needed for a large detector. Both groups invested substantial resources in scintillator development. In Figure 10 we show initial attenuation length data for the Palo Verde scintillator, which was a cocktail of 60% mineral oil, 36% pseudocumene (1,2,4 trimethylbenzene) and 4% alcohol (used to keep the Gd compound in solution), with PPO as primary fluor. This scintillator had a H:C ratio of $\simeq 2$ and a light yield of 56% of anthracene, with typical light attenuation length greater than 11 m at $\lambda = 440$ nm.[27] The time stability of the same scintillator is shown

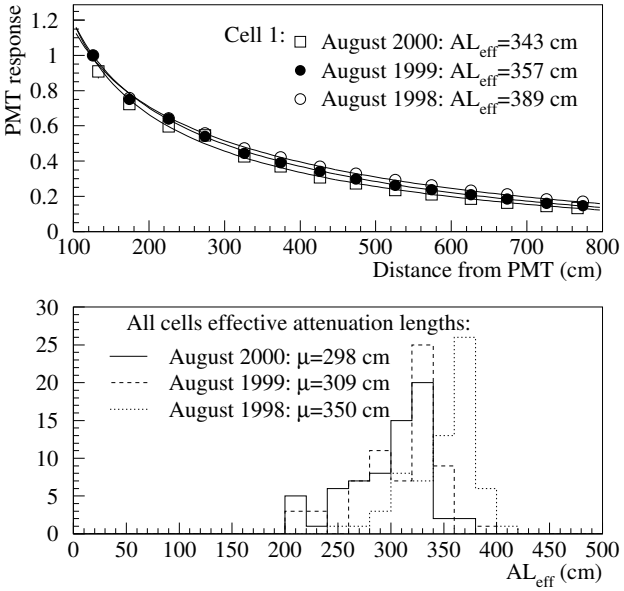

Fig. 11. Evolution of scintillation-light attenuation-length in Palo Verde scintillator during the two years of life of the detector. Top: the attenuation curve for scintillation events at different locations along one of the 9 m-long cells. Bottom: *effective* attenuation values for all detector cells. Note that the shorter value of the effective attenuation length reflects the non-trivial optics of the cells.

in Figure 11 where the light attenuation curve for one cell and the *effective* attenuation length for all cells are presented as measured three times, at one year intervals. The 12% loss in the first year decreases to 3% in the second, possibly indicating a gradual stabilization.

4.1 Chooz

The Chooz detector was built at a distance of $\simeq$ 1000 m from the two reactors of the new Chooz power plant of *Électricité de France* in the Ardenne region of France. The plant, shown in Figure 12, has a total thermal power of 8.5 GW_{th} and the two reactors reached full power in, respectively, May and August 1997. The experiment took data from April 1997 until July 1998, in the conditions specified in Table 1. The

Fig. 12. Aerial view of the Chooz power plant. The detector is located in a tunnel under the hills on the bottom right of the photograph.

detector, schematically shown in Figure 13, consisted of a central volume of 0.1% Gd-loaded scintillator with a mass of 5 tons, where $\bar{\nu}_{\rm e}$ were detected. This scintillator was contained in an acrylic vessel which separated it from a 70 cm thick shielding layer of mineral oil. 192 eight-inch photomultipliers (PMT's) were mounted onto a steel vessel which in turn isolated, mechanically and optically, the central detector from the outer veto counter. The central detector had a photocathode coverage of 15% and a light yield of $\sim$ 130 photoelectrons/MeV (p.e./MeV).[28] The 90 ton veto scintillator was at least 80 cm thick and was read out with two rings of 24 eight-inch PMT's, the

	Time (h)	$\int W_{th} dt$ (GWh$_{th}$)
Total run	8761.7	
Live	8209.3	
Dead	552.4	
Reactor 1 ON only	2058.0	8295
Reactor 2 ON only	1187.8	4136
Both reactors ON	1543.1	8841
Both reactors OFF	3420.4	0

Table 1. Summary of the Chooz data-taking conditions.

outer containment tank being painted with white reflective paint. An outer layer (75 cm thick) of low-activity sand provided primary shielding from the rock. Laser flashers were installed to monitor the detector performance and radioactive sources could be inserted into the central region of the detector through special pipes. The detector energy response was calibrated daily with ^{60}Co, ^{252}Cf and AmBe γ- and n-sources in order to accurately track the aging of the scintillator. As an example we show in Figure 14 the results of a Cf calibration run with the source placed in the middle of the detector. Data is compared with a Monte Carlo simulation for the reconstruction of the x, y and z positions and total energy in the detector. Both the peaks for n-captures on p (2.2 MeV) and Gd (8 MeV) are clearly visible. The very good energy resolution ($\sigma(E)/E = 5.6$ % at 8 MeV) allows one to verify that the 8 MeV line is in fact the superposition of a 7.77 MeV line with 77% weighting from capture on ^{157}Gd and a 8.31 MeV line with 23% weighting from capture on ^{155}Gd. The fit to these two Gaussians gives $\chi^2/\mathrm{d.o.f.} = 67.6/55$ while the fit to a single Gaussian is very poor with $\chi^2/\mathrm{d.o.f.} = 875/58$. The position resolution was found to be $\sigma_x = 17.5$ cm.

4.2 Palo Verde

The Palo Verde experiment was built at the Palo Verde Nuclear Generating Station, the largest nuclear plant in the Americas, ~ 80 km west of Phoenix, in the Arizona desert. The total thermal power from three identical pressurized water reactors is 11.6 GW. Two of the reactors were located 890 m from the detector, while the third was at 750 m. The shallow underground bunker housing the detector is shown in Figure 15 at the

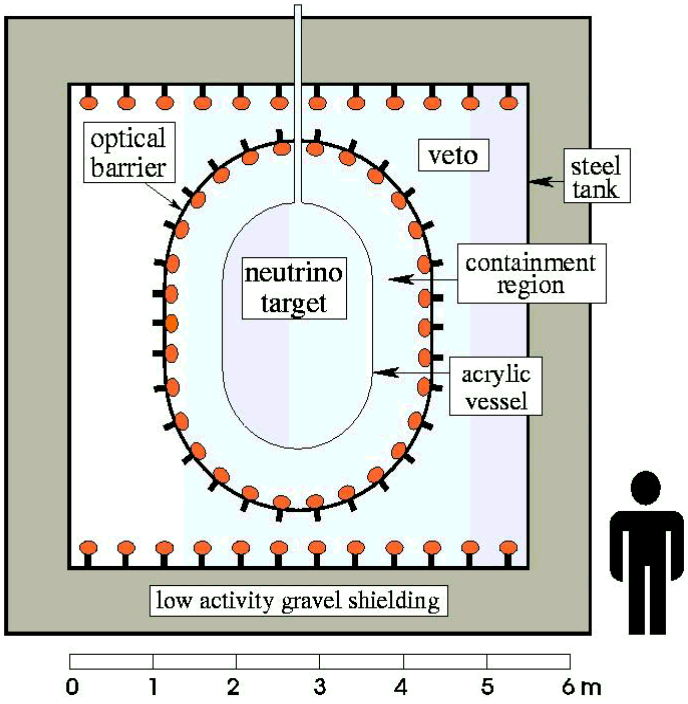

Fig. 13. Schematic drawing of the Chooz detector.

time of construction. In total 353.10 days of $\bar{\nu}_{\rm e}$ data were collected at Palo Verde in the period between October 1998 and July 2000, covering four scheduled refueling outages as indicated in Figure 9 above. 243.65 days were at full power while 22.25 days (87.19 days) had the reactor(s) at 750 m (890 m) off. This data was complemented by frequent calibration runs.

The fiducial mass, segmented for active background rejection, consisted of 66 acrylic tanks filled with 0.1% Gd-loaded scintillator and arranged as shown in Fig. 16. Each cell was 9 m long, with a 12.7×25.4 cm^2 cross section, and it was viewed by two 5-inch photomultiplier tubes, one at each end. A $\bar{\nu}_{\rm e}$ is identified by space- and time-correlated $\rm e^+$ and n signals. Positrons deposit their energy in a scintillator cell and annihilate, yielding two 511 keV γ's that, in general, will be detected in different cells, giving a triple coincidence. Neutrons thermalize and are captured in Gd, giving a γ-ray shower of 8 MeV total energy also detected in more than one cell. The central detector was surrounded by a 1 m-thick water shield to moderate background neutrons produced by muons outside the detector and to absorb γ's from the laboratory walls. Outside

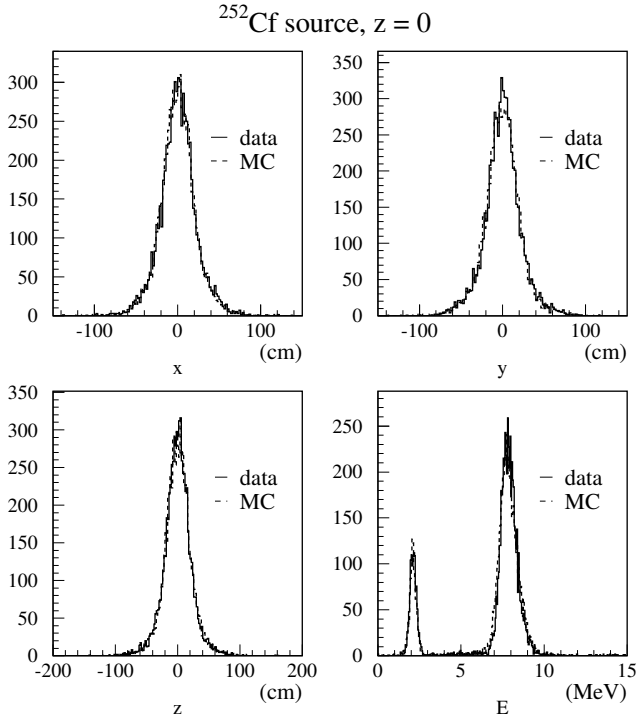

Fig. 14. Visible energy and position reconstructed for a calibration ^{252}Cf source placed inside the Chooz detector.

of the water tanks were 32 large liquid scintillator counters and two end-caps to veto cosmic muons. The rate of cosmic muons was approximately 2 kHz. The pattern of muons traveling through veto counters and their timing relative to the central detector hits were recorded for subsequent off-line analysis. The central detector was equipped with a system of tubes which allows the insertion of calibration sources in the small spaces between cells. In addition, a set of blue LEDs and optical fibers was used to produce flashes of light inside each of the cells. In order to reduce natural radioactivity, all building materials for the detector were carefully selected, including the aggregate (marble) used in the concrete of the underground laboratory.

Both the positron and the neutron were triggered by a triple coincidence requiring at least one cell above a "high" threshold set at about 600 keV (positron ionization or neutron shower core), and two cells above a "low" threshold set at about 40 keV (Compton scattering from annihilation photons or neutron shower tails). The triple coincidences were required to be within 3×5 matrixes anywhere in the detector as

Fig. 15. The Palo Verde underground laboratory at the time of construction (Fall 1996).

recognized by a custom-made trigger processor.[29]

The efficiency calibration was based upon a primary measurement performed a few times per year with a calibrated ^{22}Na e^+ source and an Am-Be neutron source. The ^{22}Na source was placed in the calibration pipes, mimicking the effects of the positron from the $\bar{\nu}_e$ interaction by providing annihilation radiation and a 1.275 MeV photon which simulates the e^+ ionization in the scintillator. The source was placed at 18 positions in the detector deemed to be representative of different conditions. The results of this procedure were then rescaled to the e^+ case using a Monte Carlo simulation. A final calibration using a ^{68}Ge source dissolved in the scintillator of one cell was performed at the end of the data-taking. The neutron detection efficiency was measured by scanning the detector with an Am-Be source where the 4.4 MeV γ associated with the neutron emission was tagged with a miniaturized NaI(Tl) counter. Other calibrations, used to measure the detector energy response, were performed using the Compton edges from ^{137}Cs, ^{65}Zn and ^{228}Th sources. The same Th source was also used more frequently to track the scintillator transparency, as already shown in Figure 11. Weekly runs of the fiber-optic and LED flasher systems were used, respectively, to monitor the gain and linearity of photomultipliers and the timing/position relationship along the cells.

Since the energy deposition of the 511 keV γ's in one cell has a sharply falling spec-

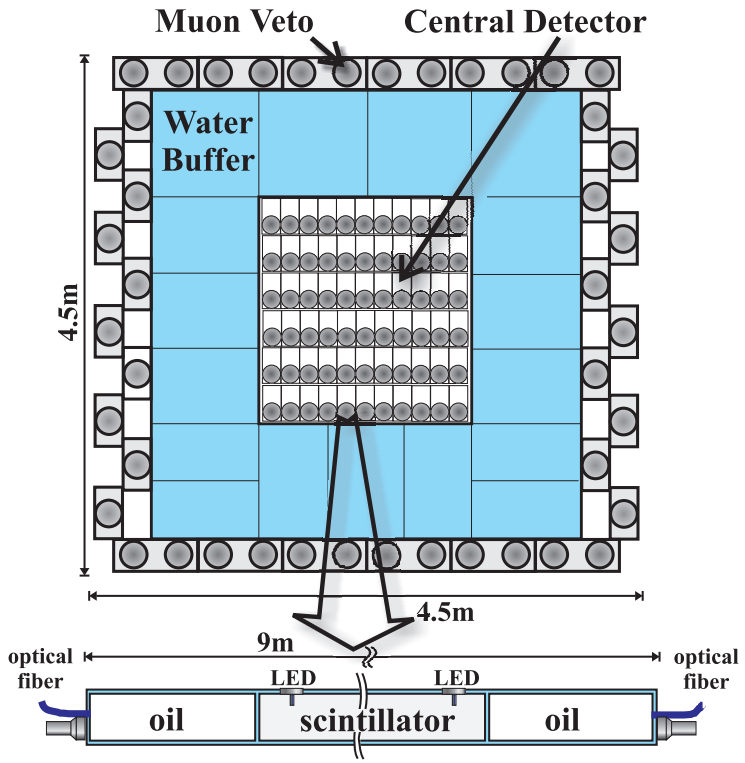

Fig. 16. Schematic view of the Palo Verde neutrino detector.

trum (Compton scattering) it was vital to have the lowest possible "low" thresholds in the trigger and to understand the behavior of such thresholds with great accuracy. This second task was complicated by the fact that the trigger used voltage amplitudes, while only charge from integrating ADCs was available off-line. For this reason the detector simulation included a detailed description of the signal development in time. This code correctly described the shape of pulses, taking into account scintillator light yield, attenuation length and de-excitation time; photomultiplier rise-time, fall-time and gain; and event position along a cell. The simulation of the detector response to the ^{22}Na source is shown in Figure 17 and correctly describes the 40 keV (600 keV) threshold position to within 1.4 keV (2.6 keV), resulting in an uncertainty on the positron (neutron) efficiency of 4% (3%).

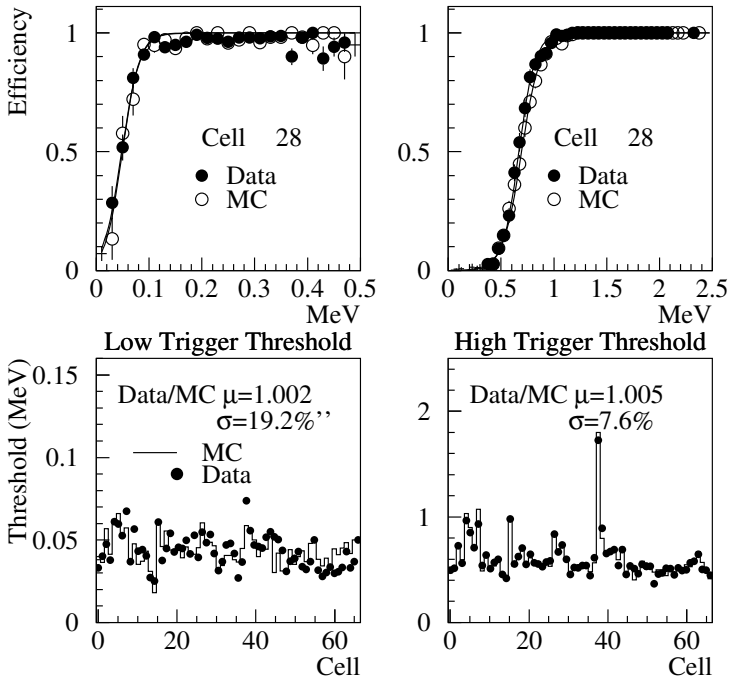

Fig. 17. A comparison of the trigger thresholds from data and Monte Carlo. The data were taken with a ^{22}Na source at the center of each cell. The top portion shows the efficiency of the trigger thresholds (low and high) for a typical cell as a function of energy deposited; the bottom shows the energy at 50% efficiency for low and high thresholds in all 66 cells.

4.3 Backgrounds

There are generally two types of background affecting long baseline reactor experiments: uncorrelated hits from cosmic-rays and natural radioactivity, and correlated ones from cosmic-μ-induced neutrons. The first type can be measured by studying the time difference between positron-like and neutron-like parts of an event. More insidious are cosmic-μ-induced neutrons, which present the same time correlation between prompt and delayed parts of the event as in $\bar{\nu}_{\rm e}$. Such events are schematically shown in the Palo Verde detector, in Figure 18. Neutrons are produced by cosmic-μ spallation and capture on the materials outside the veto counter. Both production mechanisms can result in either neutron thermalization and capture, where the thermalization process fakes the prompt triple coincidence, or secondary neutron production, where one of the captures fakes the prompt triple coincidence. Conceptually the same situation holds for

Chooz (and KamLAND, as will be discussed later), although differences in overburden and the simpler scheme of coincidence, numerically change the relative importance of different backgrounds. It is useful to point out that direct neutrons from the reactors have a totally negligible effect at the distances discussed here.

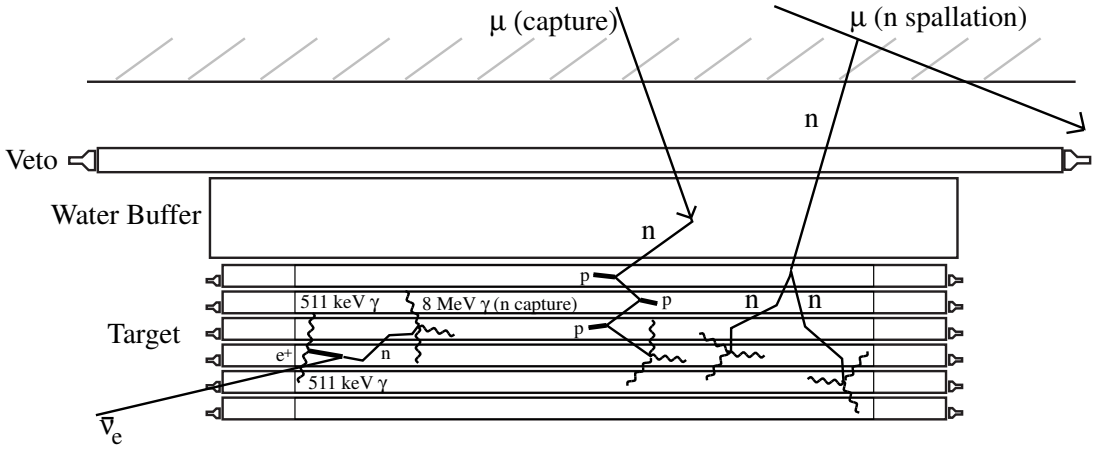

Fig. 18. Schematic view of two types of cosmic-μ-induced backgrounds compared with a signal event (far left) in the Palo Verde detector. Neutrons are produced by cosmic-μ spallation (right) and capture (left) on the materials outside the veto counter. Both production mechanisms can result in either neutron thermalization and capture (left), where the thermalization process fakes the prompt triple coincidence, or secondary neutron production (right), where one of the captures fakes the prompt triple coincidence. The μ represented to the left is an example of veto inefficiency, higher for the case of μ stopping in the detector (only one hit in the veto counter). A conceptually similar situation holds for Chooz, where, while the rate of cosmic-μ-induced events is substantially lower, events are only tagged as double coincidences.

Both experiments pre-select $\bar{\nu}_{\rm e}$ candidates by requiring an appropriate topology (in space and time) for the prompt and delayed parts of each event and their relative position. Such cuts insure that the spatial and temporal extents of the events are compatible with the $\bar{\nu}_{\rm e}$ hypothesis and that events are well contained and measured in the detector. A general classification in terms of signal and different backgrounds can be conveniently done by studying the correlation between prompt and delayed energy in Chooz for such a pre-selected sample, as shown in Figure 19. The region marked "B" in the Figure contains cosmic-ray muons stopping in the detector after entering undetected by the veto counter. Both prompt energy (muon ionization) and delayed energy (Michel electron) are large. Indeed events in region "B" show a fast time correlation between prompt and delayed part, consistent with the muon lifetime. Region "C" is populated

by the muon-spallation events discussed above: large prompt energy deposit from proton recoils in neutron thermalization is accompanied by a fixed 8 MeV energy deposit characteristic of neutron capture. Regions "A" and "D" are populated by random coincidences of natural radioactivity hits, sometimes including a high-energy proton recoil from neutron scattering in the delayed part (region "A"). Neutrino candidates populate the region framed by the darker line, as can be seen by comparison between the scatter plots with reactors ON and OFF.

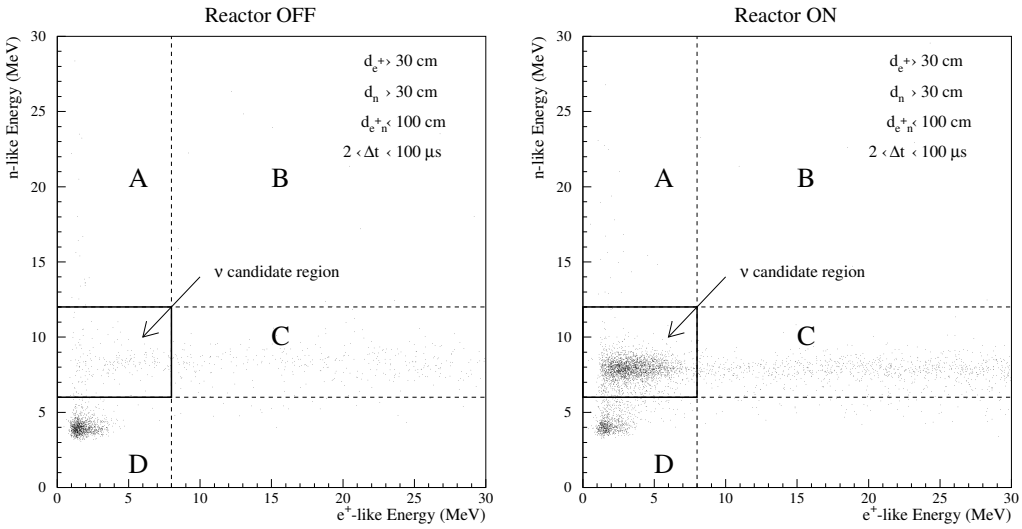

Fig. 19. Delayed energy vs. prompt energy in pre-selected Chooz events. The selection cuts are listed in the figure. On the left is shown the case of reactors OFF, while on the right is the case of reactors ON. A description of the event-types in the different regions of the plot is given in the text.

The time elapsed between the prompt and delayed parts of the events is shown in Figure 20 for the Palo Verde data. We note that the process of n-capture in the segmented detector requires the sum of two exponentials to be fit properly. This is due to the fact that a fraction of the neutrons stop, after thermalization, in passive materials (mainly acrylic for Palo Verde) where there is no Gd and the capture is a slower process. While the Monte Carlo gives a good fit with two exponentials, for data a third exponential, with longer time constant, is needed in the fit. This exponential accounts for events initiated by an uncorrelated background, having the delayed part triggered by cosmic rays, crossing the detector with a 2 kHz rate. Timing cuts are applied by both experiments to insure that events are consistent with a neutron capture. In addition

events are rejected for a period of time following tracks detected in the veto counters. This last cut is particularly important at Palo Verde where the cosmic-ray rate is high.

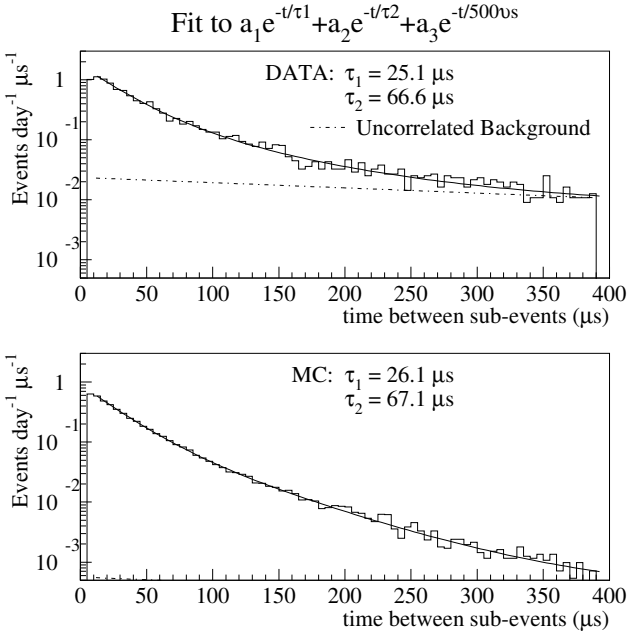

Fig. 20. Time elapsed between the prompt and delayed parts of events in Palo Verde data and Monte Carlo. The simulated data are fit to two exponentials. Data are fit to three exponentials of which the third accounts for the random background.

The availability for Chooz of data at zero power and with the reactors ramping up provides, of course, an independent way to check the magnitude of backgrounds, as shown in Figure 21 where all cuts were applied. The background estimate from the Figure is 1.1 ± 0.25 events/day. A simple subtraction of the e^+ spectra with reactor ON and OFF gives for Chooz the spectrum shown in Figure 22. The comparison of the observed distribution with the expected one for no-oscillations already shows very good agreement.

The same procedure can be repeated for Palo Verde using the thermal power excursions due to refueling. However in this case this technique substantially magnifies the errors since: 1) the periods of low power still have about 2/3 of the full flux, so that in the subtraction most of the signal is lost, 2) the statistical errors are dominated

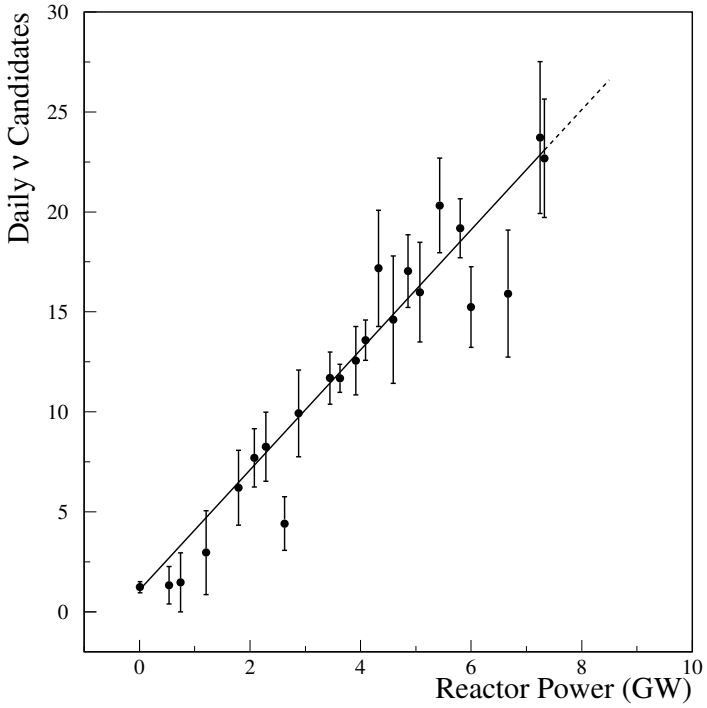

Fig. 21. Chooz data during the reactors commissioning. The background at reactors off is of 1.1 ± 0.25 events/day.

by the relatively short periods of low power. In addition, for any experiment, the subtraction used above is only justified under the assumption that the data quality (and, particularly, the efficiencies for signal *and* backgrounds) remains constant through the experiment. An alternative method[30] was developed for the Palo Verde analysis, starting from the evidence that, for their depth and detector configuration, the dominant correlated background has at least two neutrons, each triggering the detector with its capture. Such intrinsic symmetry can be used to cancel most of the background directly from data and compute the remaining components from Monte Carlo simulations. This technique makes the best possible use of the statistical power of all data collected. The rate of candidate events after all cuts can be written as $N = B_{\rm unc} + B_{\rm nn} + B_{\rm pn} + S_\nu$, where the contribution of the uncorrelated $B_{\rm unc}$, two-neutron $B_{\rm nn}$ and other correlated backgrounds $B_{\rm pn}$ are explicitly represented, along with the $\bar{\nu}_{\rm e}$ signal S_ν. The dominant background $B_{\rm nn}$ (along with $B_{\rm unc}$) is symmetric under exchange of sub-events, so that an event selection with the requirements for the prompt and delayed event parts

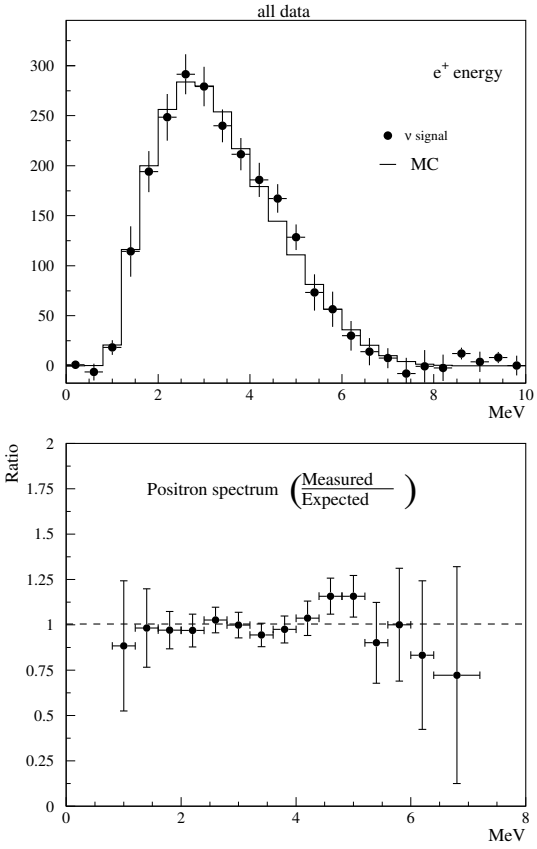

Fig. 22. Background subtracted positron energy spectrum in Chooz data. Error bars represent statistical errors only. The solid histogram represent the expectation for the case of no oscillations. The ratio between the two curves is shown on the bottom panel.

swapped, will result in a rate $N' = B_{\rm unc} + B_{\rm nn} + \epsilon_1 B_{\rm pn} + \epsilon_2 S_\nu$. Here ϵ_1 and ϵ_2 account for the different efficiency for selecting asymmetric events after the swap. One can then calculate $N - N' = (1-\epsilon_1)B_{\rm pn} + (1-\epsilon_2)S_\nu$ where the efficiency correction $\epsilon_2 \simeq 0.2$ can be estimated from the $\bar{\nu}_{\rm e}$ Monte Carlo simulation. The Palo Verde group found that the processes of μ-spallation in the laboratory walls and capture of the μ's that are not tagged by the veto counter, contribute to $(1-\epsilon_1)B_{\rm pn}$, while other backgrounds are negligible. Using Monte Carlo simulation, they obtain $(1-\epsilon_1)B_{\rm pn} = -0.9 \pm 0.5$ d^{-1} (-1.3 ± 0.6 d^{-1}) for μ-spallation in the 1998 (1999) data-set; the same figures for μ-capture are 0.6 ± 0.3 d^{-1} (0.9 ± 0.5 d^{-1}) in 1998 (1999). This represents only a small correction to $N - N'$ since the error on $B_{\rm pn}$ is de-magnified by the fact that ϵ_1 is close

to 1. While the Monte Carlo model is accurate for the capture process, in the case of spallation the broad range of spectral indexes for the n-recoil energy reported in literature was simulated.[30] The average between different predictions is then used for $B_{\rm pn}$ while the spread is used as an extra systematic error. Since no $\bar{\nu}_{\rm e}$ signal is present above 10 MeV, the observed integrated rate above this energy is used as a normalization of the Monte Carlo.

The Palo Verde results obtained in this way are shown in Table 2 for different running periods. Clearly also in this case there is good agreement with the no-oscillation hypothesis.

Period	98 "on"	98 "off"*	99 "on"	99 "off"†
Duration (d)	36.0	31.3	111.0	23.4
η	0.0746	0.0772	0.112	0.111
N (d^{-1})	38.2 ± 1.0	32.2 ± 1.0	52.9 ± 0.7	43.9 ± 1.4
S_ν (d^{-1})	16.5 ± 1.4	13.4 ± 1.4	25.2 ± 0.9	15.1 ± 1.9
B (d^{-1})	21.7 ± 1.0	18.8 ± 1.0	27.7 ± 0.6	28.8 ± 1.3
$R_{\rm Obs}$ (d^{-1})	221 ± 18	174 ± 17	225 ± 8	136 ± 17
$R_{\rm Calc}$ (d^{-1})	218	155	218	130

Table 2. Summary of results from the Palo Verde experiment. * Reactor at 890 m distance off. † Reactor at 750 m distance off. Statistical uncertainties only.

4.4 Results and systematics

A summary of systematic errors for both Chooz and Palo Verde is given in Table 3. Although the Table does not include the final calibration at Palo Verde, the systematic error given for Chooz should probably be considered as some sort of ultimate limit for reactor-based oscillation experiments, at least when only one detector is present. Indeed the intrinsically high efficiency ($\simeq 70\%$) of the homogeneous detector, together with the unique opportunity of studying the zero power case, are important advantages (for comparison the efficiency of the larger but segmented Palo Verde detector is $\simeq 11\%$).

The (energy averaged) ratio between $\bar{\nu}_{\rm e}$ detected and expected was found to be

$$R = 1.01 \pm 2.8\%({\rm stat}) \pm 2.7\%({\rm syst}) \qquad {\rm Chooz} \tag{8}$$

and

$$R = 1.04 \pm 3\%(\mathrm{stat}) \pm 8\%(\mathrm{syst}) \qquad \mathrm{PaloVerde} \tag{9}$$

in both cases consistent with 1.

Systematic	Chooz (%)		Palo Verde (%)	
$\sigma(\bar{\nu}_{\mathrm{e}} + \mathrm{p} \rightarrow \mathrm{n} + \mathrm{e}^{+})$	1.9		-	
Number of p in target	0.8		-	
$P_t h$	0.7		-	
Energy absorbed per fission	0.6		-	
Total rate prediction		2.3		3.0
e^{+} det. eff.	-		4.0	
n det. eff.	-		3.0	
$\bar{\nu}_{\mathrm{e}}$ selection cuts	-		4.0	
B_{pn} estimate	-		4.0	
Total $\bar{\nu}_{\mathrm{e}}$ efficiency		1.5		7.5
Total		2.7		8.0

Table 3. Origin and magnitude of systematic errors in Palo Verde and Chooz. Note that the two experiments offer different breakdowns of their systematics. For simplicity we do not show the systematics for the Palo Verde ON-OFF analysis. As usual the Palo Verde results only include the first half of their data set and do not include the final detector calibration.

Both experiments were able to exclude $\bar{\nu}_{\mathrm{e}}$ - $\bar{\nu}_{\mathrm{X}}$ oscillations as being mainly responsible for the atmospheric neutrino anomaly. This is evident from the exclusion contours obtained by both experiments using the unified approach[31] and shown in Figure 23 for Chooz and Figure 24 for Palo Verde.

4.5 Are smaller mixing angles within experimental reach ?

The current data on neutrino oscillations suggests the need to include at least three neutrino flavors when studying results from experiments. The most general approach would involve five unknown parameters, three mixing angles and two independent mass differences. However, an intermediate approach consists of a simple generalization of the two flavor scenario, assuming that $m_3^2 \gg m_1^2, m_2^2$ (i.e. $\Delta m_{13}^2 = \Delta m_{23}^2 = \Delta m^2$, while $\Delta m_{12}^2 \simeq 0$). In such a case the mixing angle θ_{12} becomes irrelevant and one is

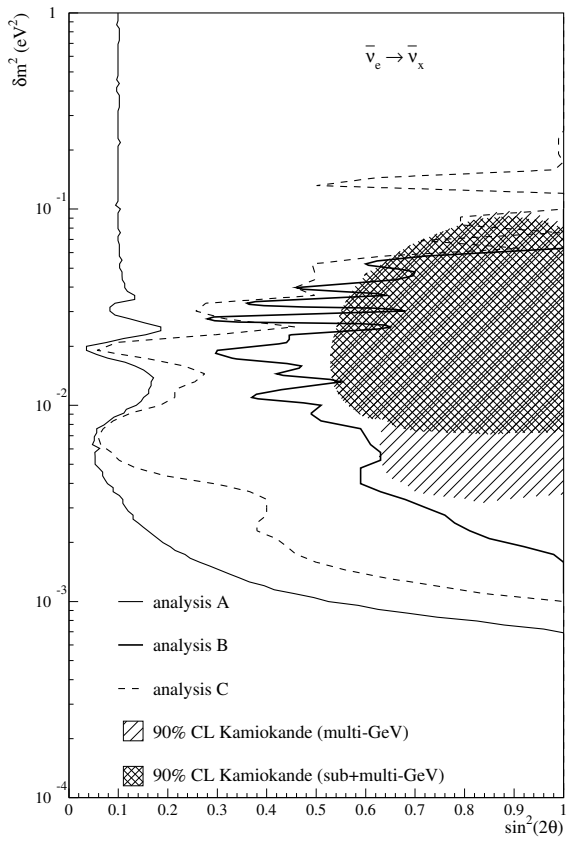

Fig. 23. Limits on mass difference and mixing angle from Chooz (90% CL) obtained with the unified approach.[31] Analysis A refers to the curve obtained by a fit to the background-subtracted spectrum in which both shape and normalization are used. Analysis C uses only the shape of the spectrum. Finally analysis B uses the difference of baselines between the two reactors ($\Delta L = 116.7$ m). While in this last case most systematics cancel, the statistical errors are larger, and the Δm^2 sensitivity rather poor due to the short baseline difference. The Kamiokande $\nu_{\rm e} - \nu_\mu$ atmospheric neutrino result is also shown.

left with only three unknown quantities: $\Delta m^2, \theta_{13}, \text{and } \theta_{23}$. With this parameterization, and assuming that ν behave like $\bar{\nu}$, the $\bar{\nu}_e$ disappearance is governed by

$$P(\bar{\nu}_e \to \bar{\nu}_x) = \sin^2 2\theta_{13} \sin^2 \frac{\Delta m^2 L}{4E_\nu} \ , \tag{10}$$

while the $\nu_\mu \to \nu_\tau$ oscillations, assuming that this scenario is responsible for the atmospheric neutrino results, are described by

$$P(\nu_\mu \to \nu_\tau) = \cos^4 \theta_{13} \sin^2 2\theta_{23} \sin^2 \frac{\Delta m^2 L}{4E_\nu} \ . \tag{11}$$

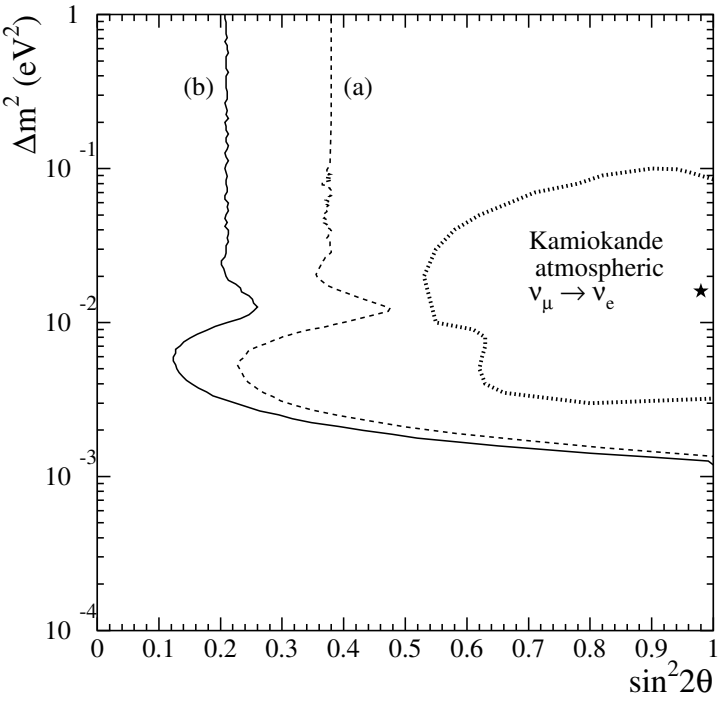

Fig. 24. Limits on mass difference and mixing angle from Palo Verde (90% CL) obtained with the unified approach.[31] Curve (a) is obtained by using the reactor power changes to estimate and subtract the background, while curve (b) is obtained with the alternative background subtraction method described in the text. The Kamiokande $\nu_\mu - \nu_e$ atmospheric neutrino result is also shown.

A preliminary analysis of the atmospheric neutrino data based on these assumptions has been performed[32] and its results are shown in Figure 25 for the ν_e disappearance channel. One can see that, while the relevant region of the mass difference Δm^2 is determined by the atmospheric neutrino data, the mixing angle θ_{13} is not constrained very much. Here the reactor-based neutrino oscillation experiments play a decisive role.

It is interesting to ask whether such a role can be extended to address regions of even smaller mixing parameter $\sin^2 2\theta_{13}$. A simple inspection of Table 3 shows that, using the Chooz systematics, if all flux and cross-section related errors could be set to zero one would be left with an error of $\simeq 1.5\%$. Assuming a detector large enough to produce negligible statistical error the total error would shrink from the present 3.9% to 1.5%.

This scenario is considered by Ref. 15, which proposes to use an underground reac-

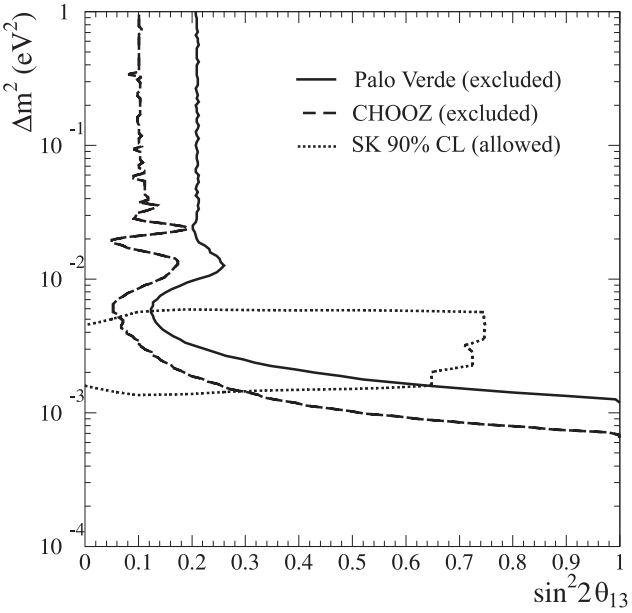

Fig. 25. Exclusion plot showing the $allowed$ region of θ_{13} and Δm^2 based on the Super-Kamiokande preliminary analysis (the region $inside$ the dotted curve). The region $excluded$ by the neutrino reactor experiments is to the right of the corresponding dashed and continuous curves.

tor at Krasnoyarsk in Russia as a source, and two identical detectors placed at distances of $\simeq 1100$ m and $\simeq 250$ m. The interesting feature of the Krasnoyarsk site is that there are substantial facilities available underground, with an overburden of ~ 600 m.w.e., twice the depth of Chooz. Indeed it might even be conceivable to locate the detectors on rail-cars and periodically switch their position to further reduce some of the systematics related to detector efficiency. The proposal discusses the use of 50 tons of Gd-loaded scintillator for each of the two homogeneous detectors, so that the far detector would collect 50 events/day (the thermal power of the reactor is in this case lower than at Chooz or Palo Verde. The background is estimated to be 5 events/day or less.

This proposal estimates that such an experiment could reach a sensitivity in mixing strength of better than 0.02 in the Δm^2 region relevant for atmospheric neutrinos. While the idea certainly looks interesting, it would be useful to explore how practical it is in general to push the errors of the absolute $\bar{\nu}_{\rm e}$ flux to the 1% domain, even with the measurements considered here. Finally one should understand the schedule for operation of the Krasnoyarsk reactors which, according to the Gore-Chernomyrdin[33] agreement, are supposed to be shutdown for re-coring in some future.

5 Exploring the solar ν anomaly on earth: KamLAND

While historically solar neutrinos have provided us with the first hint for oscillations, most people consider today that the strongest evidence for oscillation is provided by the atmospheric neutrino anomaly. Indeed the azimuthal dependence of the anomaly has substantially helped to reduce the effect to some property of neutrinos, and the advent of K2K, to be followed soon by the Minos and CERN to Gran Sasso programs,[9] are bringing the study of oscillations in this regime to a laboratory activity with both source and detector well under control.

While in the case of solar neutrinos none of the effects that would be generally considered "smoking guns" for oscillations has clearly emerged from the data, their exploration "in a laboratory setting" is made particularly challenging by the huge L/E_ν required. It is probably a safe prediction that it will take a very long time before an accelerator-based experiment will be able to tackle the solar neutrino problem! However, the very low energy of reactor neutrinos make a reactor-based oscillation experiment able to reach the Large Mixing Angle (LMA) MSW solution possible — albeit rather challenging. While we prefer to leave to others the assessment of how likely this solution is to be the right one, we find the chance to study solar neutrino oscillations "in the lab" absolutely amazing and compelling. We note here that, unlike in the case of atmospheric neutrinos, where it turned out that electron neutrinos were not involved in the dominant mixing, the solar neutrino problem, if due to oscillations, has to be related to $\nu_{\rm e}$ disappearance. So, unless $\bar{\nu}_{\rm e}$ behave drastically differently from $\nu_{\rm e}$ (which would be a worthwhile discovery anyway!) a reactor experiment is an exact replica of the astrophysical experiment, only built on earth.

5.1 Nuclear reactors in Japan

The "easier" solution of the solar neutrino problem (LMA MSW) is shown in Figure 1. In order to completely explore this solution one needs a Δm^2 sensitivity of at least 10^{-5} eV^2 at large mixing angle. As is now customary we refer to Figure 3 as a first step in designing our experiment: we see that a ≈ 100 km baseline is needed and this drives the power$\times$fiducial-mass product between 10^7 and 10^9 $\mathrm{MW_{th}} \times \mathrm{tons}$. Clearly a large detector has to be used in conjunction with very many nuclear reactors. A cursory look at the placement of nuclear power plants on the earth, Figure 26, reveals that such an experiment could only be placed in Europe, the eastern United States, or Japan.

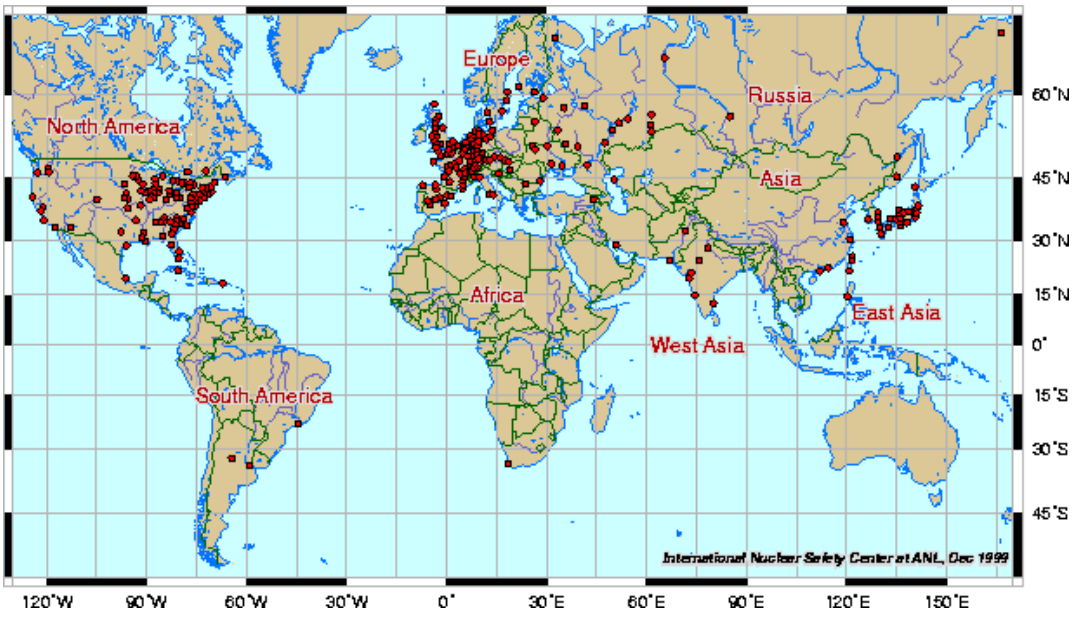

Fig. 26. Location of nuclear power plants in the world. Substantial concentrations of reactors are in Europe, the eastern US, and Japan.

There are 16 commercial nuclear power plants in Japan, their location being shown in Figure 27. They supply about 1/3 (or 130 $\mathrm{GW_{th}}$) of the total electric power in the country. At the Kamioka site there is an anti-neutrino flux of $\simeq 3 \times 10^6\,\mathrm{cm^{-2}s^{-1}}$ (or $\simeq 1.3 \times 10^6\,\mathrm{cm^{-2}s^{-1}}$ for $E_{\bar{\nu}} > 1.8$MeV) from these reactors. 80% of this flux derives from reactors at a distance between 140 km and 210 km, so that there is a limited range of baselines. The breakdown of this data by power plant (several plants have on site more than one reactor) is given in Figure 28. We note that some 2% of the flux derives from power plants in South Korea that will have to be included (albeit only as a crude estimate) to provide an exact flux prediction.

While the table in Figure 28 assumes the nominal power for each of the cores, an average over one year, taking into account scheduled and unscheduled down times, gives an expected non-oscillation rate of $\simeq$750 $\mathrm{kton^{-1}year^{-1}}$ for a $\mathrm{C}_n\mathrm{H}_{2n+2}$ target. Although the signal is provided by a very large number of cores, it turns out that a modulation of the $\bar{\nu}_\mathrm{e}$ flux is expected at KamLAND[34] thanks to the refueling and maintenance schedule of nuclear power plants in Japan. Such shutdowns, in fact, are concentrated in the Fall and Spring when the power demand is lowest, as illustrated in Figure 29. Hence, from the point of view of the tools available to study backgrounds, KamLAND is in a

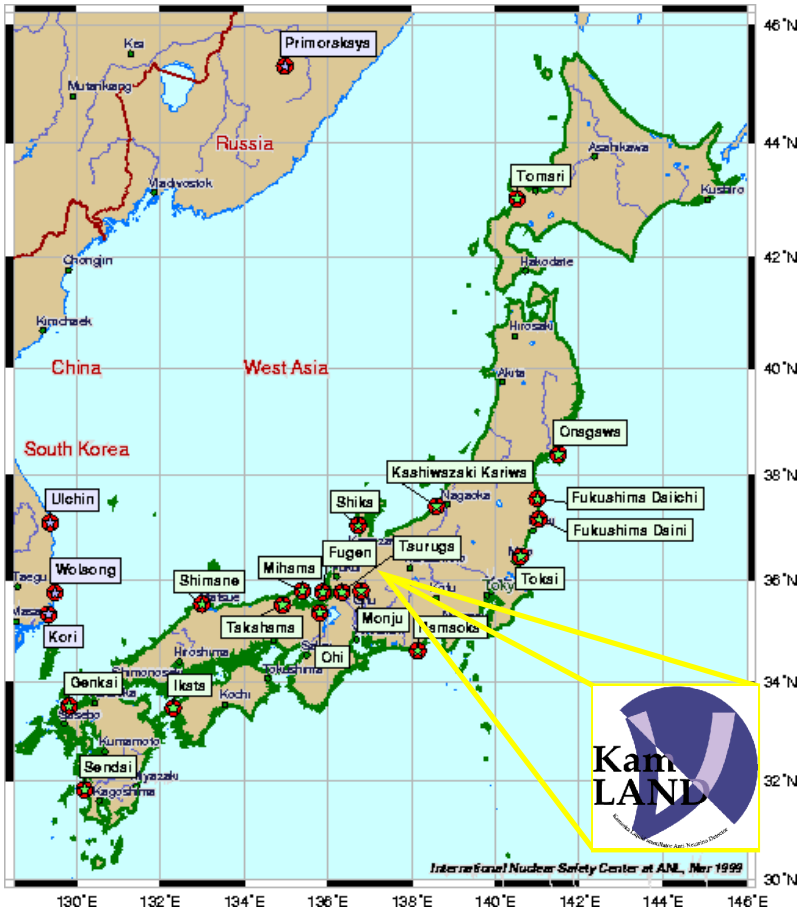

Fig. 27. Location of large nuclear power plants in Japan, Korea and eastern Russia.

situation very similar to that of Palo Verde, with 2 dips in the flux from full to $\approx 2/3$ expected every year.

5.2 Detector design

The KamLAND detector is housed in the cavity built for the Kamiokande detector under the summit of Mt. Ikenoyama in the Japanese Alps, about 50 km east of the town of Toyama. The layout of the laboratory is shown in Figure 30. The rock overburden is more than 1,000 m in any direction with an average rock density of 2.7 g/cm^3. The site is at 500 m distance from SuperKamiokande.

A cutout view of the KamLAND detector is shown in Figure 31. The fiducial volume consists of a sphere containing 1000 tons of liquid scintillator. The scintillator

Site	Distance	# of	P(ther.)	flux	Signal
Japan	(km)	cores	(GW)	($\bar{\nu}$ cm^{-2}s^{-1})	($\bar{\nu}$/yr)
Kashiwazaki	160.0	7	24.6	4.25×10^{5}	348.1
Ohi	179.5	4	13.7	1.88×10^{5}	154.0
Takahama	190.6	4	10.2	1.24×10^{5}	101.8
Hamaoka	214.0	4	10.6	1.03×10^{5}	84.1
Tsuruga	138.6	2	4.5	1.03×10^{5}	84.7
Shiga	80.6	1	1.6	1.08×10^{5}	88.8
Mihama	145.4	3	4.9	1.03×10^{5}	84.5
Fukushima–1	344.0	6	14.2	5.3×10^{4}	43.5
Fukushima–2	344.0	4	13.2	4.9×10^{4}	40.3
Tokai–II	294.6	1	3.3	1.7×10^{4}	13.7
Shimane	414.0	2	3.8	9.9×10^{3}	8.1
Onagawa	430.2	2	4.8	9.8×10^{3}	8.1
Ikata	561.2	3	6.0	8.4×10^{3}	6.9
Genkai	755.4	4	6.7	5.3×10^{3}	4.3
Sendai	824.1	2	3.3	3.5×10^{3}	2.8
Tomari	783.5	2	5.3	2.4×10^{3}	2.0
Korea					
Ulchin	~750	4	11.2	8.8×10^{3}	7.2
Wolsong	~690	4	8.1	7.5×10^{3}	5.2
Yonggwang	~940	6	16.8	8.4×10^{3}	6.9
Kori	~700	4	8.9	8.0×10^{3}	6.6
Total		69	175.7	1.34×10^{6}	1102

Fig. 28. List of relevant parameters for power reactors in Japan and South Korea.

container is a thin plastic-walled balloon of 6.5 m radius that is not supposed to take the weight of the scintillator but only to isolate it from an outer 2.5 m thick layer of non-scintillating, radiation shielding, fluid. The balloon is also designed to be impermeable to radon that mainly originates from Th and U contaminations inside the PMT's glass. The buffer fluid and the liquid scintillator are contained and mechanically supported by a stainless steel spherical vessel which also provides the mechanical structure where the photomultipliers for the fiducial volume are mounted. The sphere is solidly mounted inside the cylindrical rock cavity and the space between them is filled with water and used as a veto Čerenkov counter. The scintillator, based on mineral oil and pseudocumene, is designed to achieve sufficient light yield and n-γ discrimination by pulse-shape analysis, yet complying with rather strict flammability requirements from the Kamioka mine. Given the cost and stability issues for a detector of the size of KamLAND, it was chosen not to Gd-load the scintillator. As will be discussed later, simulations indicate that sufficient signal-to-noise ratio will be achieved with unloaded scintillator. Events will be localized inside the fiducial volume using the light propaga-

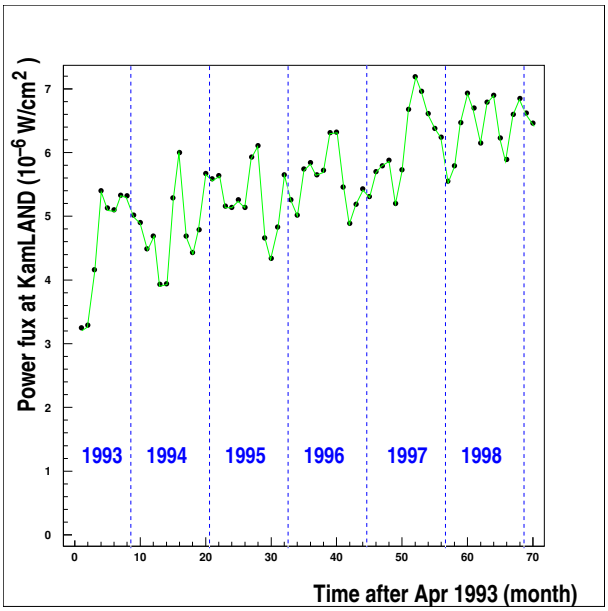

Fig. 29. Power-flux level at Kamioka from Japanese reactors as a function of time. Low power periods in the Fall and Spring seasons are alternated with peaks of high power in the Summer and Winter.

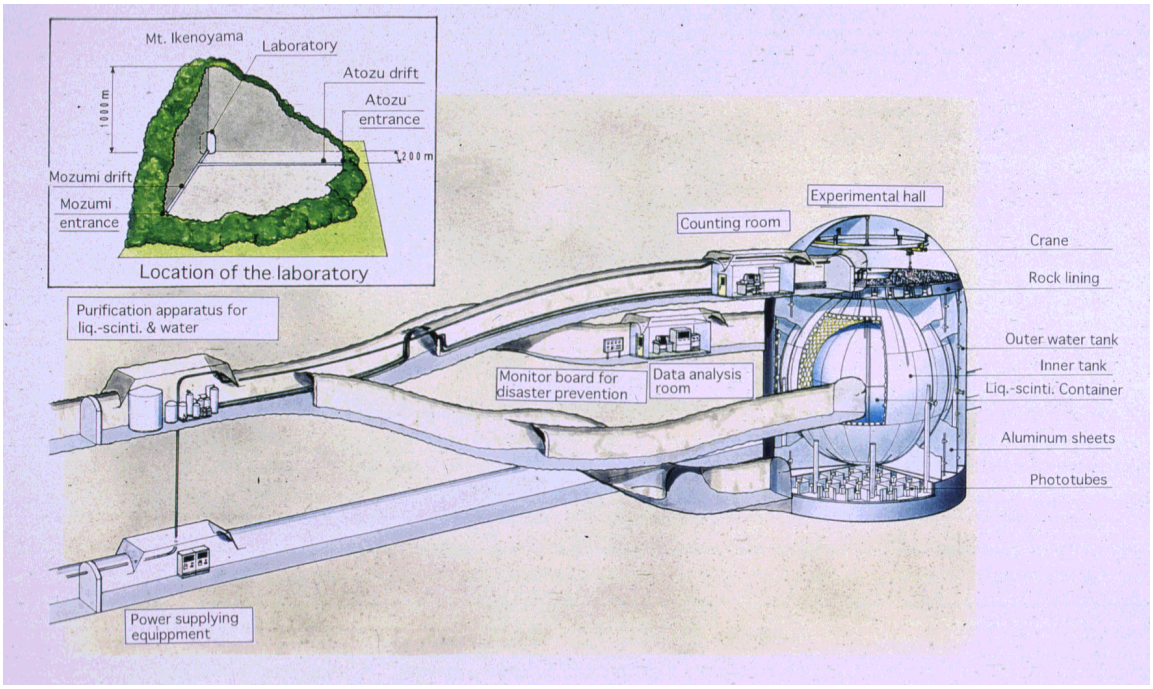

Fig. 30. Partial view of the system of tunnels inside Mount Ikenoyama with the locations of KamLAND and its main services.

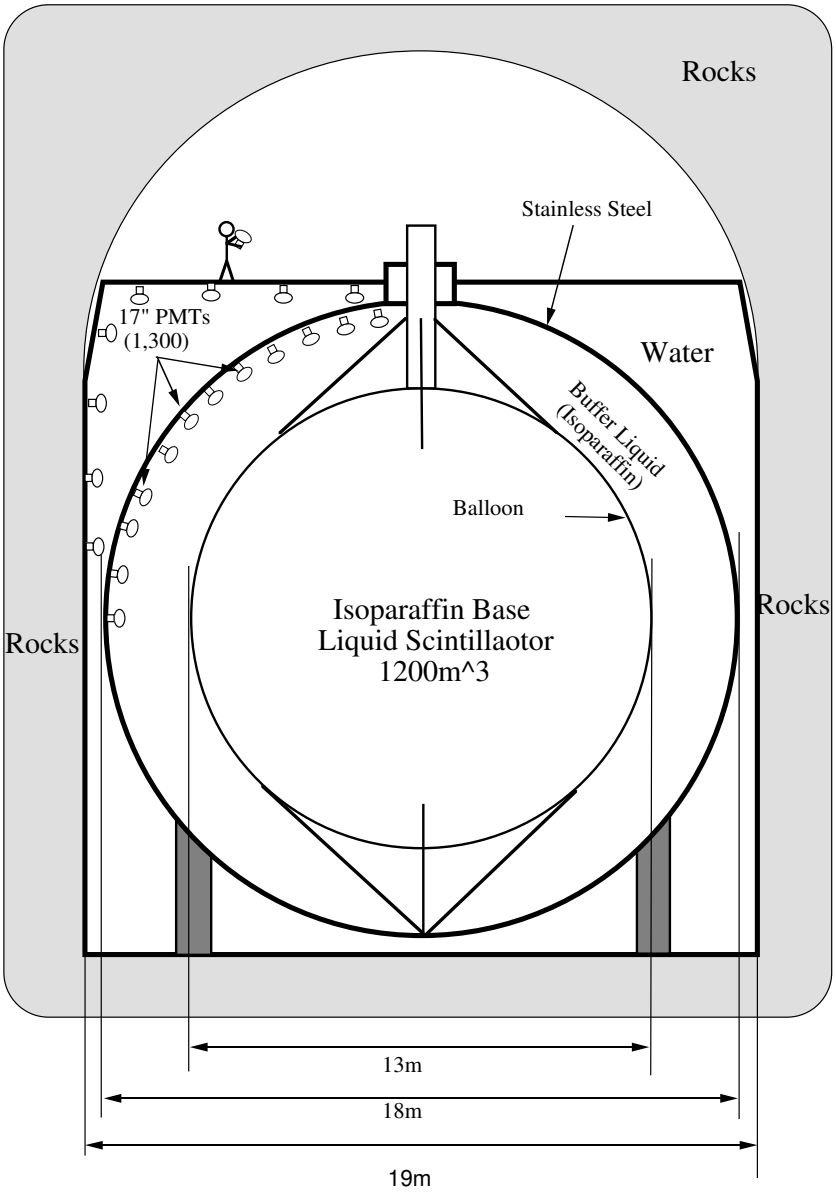

Fig. 31. Schematic cross-section of the KamLAND detector.

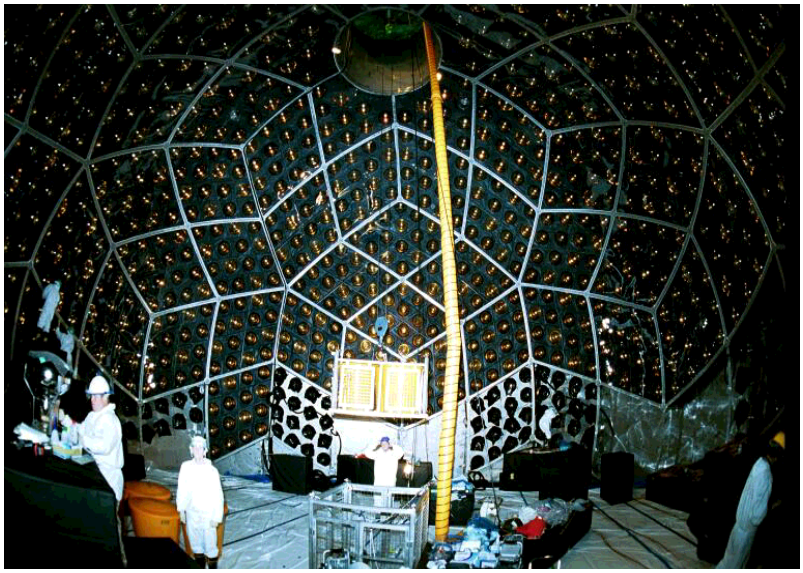

Fig. 32. View of the internal volume of the sphere during the central detector installation. A modular styrofoam raft is used as a platform for workers. The installation began from the top of the sphere and moved down, as the water level in the sphere was reduced. PMTs, black shades, acrylic plates, monitoring LEDs and cables were mounted in place for each level before lowering the water.

tion delays to the different photomultipliers so that large area, fast tubes are required. While the veto counter will be read out using 20-inch photomultipliers dismounted from the Kamiokande detector, new, faster, tubes with 17-inch active photocathode have been developed for KamLAND in order to allow for proper vertex reconstruction from timing. Such tubes have an average transit-time-spread of $\simeq 3$ ns (to be compared to $\simeq 5$ ns for the Kamiokande/SuperKamiokande tubes). The central detector has a 30% photocathode coverage obtained using about 1280 17-inch tubes complemented, for energy measurements, by 642 20-inch Kamiokande tubes. A spherical shell of acrylic panels (not shown in Figure 31) is mounted at a radius immediately inside the position of the PMT's and is used as the primary barrier against radon migration into the active scintillator. A cylindrical stainless steel chimney of 3 m diameter protrudes from the top of the sphere to permit access to the central detector during installation. Buffer fluid and scintillator lines as well as calibration ports will be mounted in the chimney along with all the electrical cabling.

The readout of KamLAND is designed to provide waveform analysis information for each of the PMT's in the detector with essentially no dead-time for several consecu-

Background source	Rate (day^{-1})
Cosmic-muon-induced neutrons	0.1
Natural radioactivity (random coincidence)	0.15
Natural radioactivity (correlated)	0.005
Total predicted background	0.25
Reactor $\bar{\nu}_e$ signal (no oscillation)	2

Table 4. Summary of background rates for the $\bar{\nu}_e$ signature. A signal-to-noise ratio of about 10/1 is expected for reactor $\bar{\nu}_e$.

tive events. This allows for clean event reconstruction and enables the off-line study of the pre-history of interesting events. For example, multiple neutron events, described above as the most dangerous background at Palo Verde, will be fully reconstructed by KamLAND. Similarly, cosmogenic activation giving short half-life nuclei will be clearly recorded. Deep digital buffering will allow the detector to sustain substantial bursts of events like that expected from supernovae.

In Figure 32 we show a phase of the central detector PMT installation that was concluded in September 2000. The KamLAND installation schedule calls for scintillator filling to start in early Spring 2001 and data taking to begin in the Summer 2001.

5.3 Expected performance

Similarly to previous experiments, both random hits from natural radioactivity, and correlated events from neutron production in cosmic-ray-muon spallation and capture, contribute to the background to reactor $\bar{\nu}_e$ in KamLAND. The results of Monte Carlo full detector simulation using the measured Kamioka cosmic ray flux and the activities of various components as sampled during construction are given in Table 4. For the purpose of this background estimate we have used U and Th contaminations in the scintillator of 10^{-14} g/g that have already been achieved in samples of the KamLAND scintillator. Monte Carlo studies have shown that cosmogenic activation gives negligible contribution to the background for doubles. A discussion of backgrounds to single signatures, not considered here, can be found elsewhere.[34]

In Figure 33 we show the predicted energy spectra for reactor neutrinos at KamLAND for no oscillations and different oscillation parameters consistent with the LMA

MSW solar neutrino solution. We can use one of these curves and add to it fluctuations consistent with a 10/1 signal-to-noise ratio and three years of data to investigate the sensitivity of the experiment. Assuming that oscillations with $\Delta m^2 = 2 \times 10^{-5}$ eV^2 and $\sin^2 2\theta = 0.75$ are indeed the cause of the solar neutrino anomaly, we obtain the measurement of the oscillation parameters shown in Figure 34. On the other hand, no evidence for oscillation after three years of data would result in the exclusion curve shown in Figure 1 and would rule out the LMA MSW solution to the solar neutrino problem.

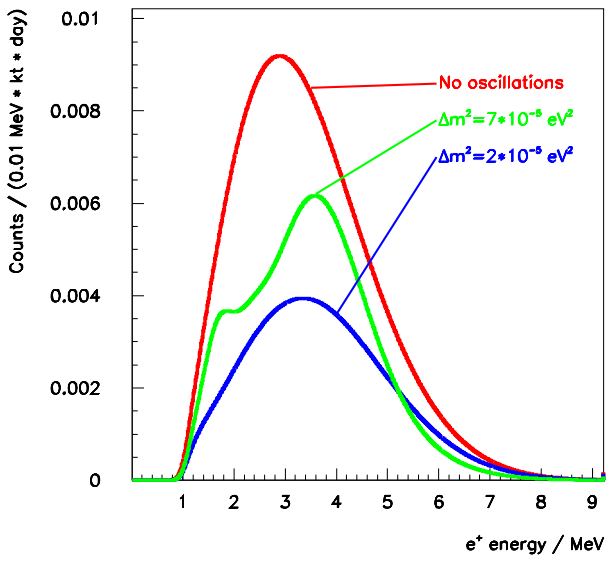

Fig. 33. Positron energy spectra expected at KamLAND for no oscillations and oscillations with parameters in the LMA MSW solar neutrino solution.

5.4 Other physics with a very large $\bar{\nu}_e$ detector

KamLAND will be the largest detector specifically optimized to detect low-energy $\bar{\nu}_e$ with good efficiency and low background. This opens a number of interesting opportunities beyond the measurement of oscillations from reactors. In addition, such a large detector with a low energy threshold can be used to directly measure neutrinos from the Sun, particularly the ^{7}Be line that is below the threshold of the water Čerenkov detectors. The presence of large amounts of carbon in KamLAND's scintillator opens the possibility of detailed flavor studies in neutrinos coming from supernovae. Finally

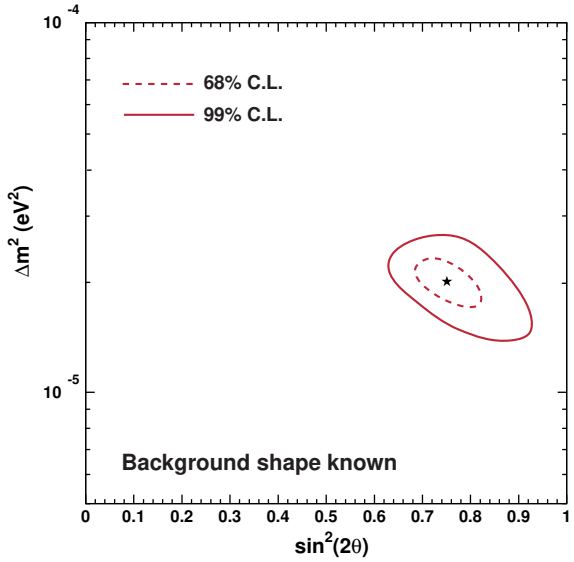

Fig. 34. Simulated measurement of neutrino oscillation parameters from three years of data at KamLAND assuming $\Delta m^2 = 2 \times 10^{-5}$ eV^2 and $\sin^2 2\theta = 0.75$. A signal-to-noise ratio of 10/1 was assumed (see text).

KamLAND represents such a large step in size and backgrounds relative to the previous detectors that we should be ready for the possibility that it will discover completely new and unexpected phenomena in physics or astrophysics.

Given our space limitations we will only mention here the topic of terrestrial $\bar{\nu}_{\rm e}$ that is somewhat unusual and directly relates to the experiment's ability to detect $\bar{\nu}_{\rm e}$'s. The reader interested in the direct detection of solar neutrinos or neutrinos from supernovae is referred to the KamLAND design report.[34] A description of the new and unexpected phenomena mentioned above will be hopefully provided at a later stage.

Although the study of terrestrial anti-neutrinos was proposed as early as 1966[35] practical difficulties, due to the very small cross-sections and very low energies involved, have made this physics impractical until now. KamLAND has the ability to detect energy depositions of the order of 1 MeV in a unprecedented amount of liquid scintillator and is therefore ideally suited for this study. It is important to realize that low energy $\bar{\nu}_{\rm e}$ are easily detected with very low background in KamLAND thanks to their very specific signature.

The cooling rate of our planet and its contents of heavy elements are central issues

in the earth sciences. The earth radiates about 40 TW of heat from its surface. About 40% of this energy (or 16 TW) is believed to have radiogenic origin with 90% of it deriving from decays of ^{238}U and ^{232}Th. Radiogenic heat is therefore an essential component of the present dynamics of our planet. As discussed by several authors,[35–37] the concentration of these isotopes can be mapped, at planetary scale, by direct detection of $\bar{\nu}_e$ deriving from the β-decay processes. Since neutrinos have a mean free path many orders of magnitude larger that the size of our planet, the neutrino field is analogous, except for directionality information, to a gravitational field, where the sources are represented by radioactive density (as opposed to mass density).

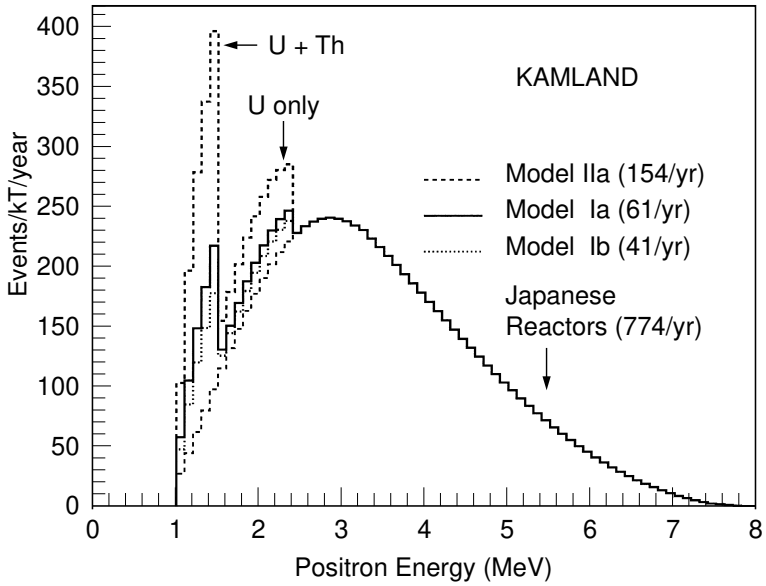

Fig. 35. Energy spectrum from terrestrial anti-neutrinos compared with reactor signal as expected in KamLAND. Three different geophysical models[38] are shown for the terrestrial anti-neutrinos and no oscillations are assumed for all the spectra shown.

Since the maximum energy carried by terrestrial neutrinos is[37] 3.27 MeV and the capture threshold is 1.8 MeV, the maximum in the energy spectrum detected in the prompt part of the events will be 2.49 MeV (including the 1.02 MeV from positron annihilations). For energies above threshold only the Thorium and Uranium decay chains give a detectable amount of events. ^{234}Pa from the U chain and ^{228}Ac and ^{212}Bi of the Th chain have similar endpoints (respectively 2.29 MeV, 2.08 MeV and 2.25 MeV) while ^{214}Bi from the U chain has an endpoint of 3.27 MeV. Therefore the energy spectrum

observed for the prompt part of the event has a characteristic double-hump structure shown in Figure 35. This will also allow the measurement of the U/Th ratio. Anti-neutrinos from nuclear reactors give, as described above, a similar signature, but their energy is substantially higher and, as shown in the Figure, they can be easily separated from the terrestrial anti-neutrinos.

The two lower spectra (Ia and Ib) superimposed in Figure 35 for the terrestrial anti-neutrino component correspond to two different possible geophysical models with different heavy elements concentration in the oceanic and continental crusts.[38] The highest curve (IIa) is given as a reference and shows what the spectrum would be in the extreme case where the entire 40 TW of heat escaping from the Earth's interior was generated by the Th and U decay chains.

In one year of data-taking, model Ia would give an integral of 61 events while model Ib would give only 41 events, and a differentiation between the two at 3σ level could be obtained in five years of data-taking, taking into account the fluctuations of the background due to the reactor neutrinos.

6 Conclusions

The use of nuclear reactors to study neutrino properties has a long and glorious history. While the first experiments devoted to oscillation searches were motivated by the generic principle to "look where the light is", many of the modern hints for neutrino oscillations point to parameters that match very well the capabilities of reactor-based experiments. At the same time the understanding of the flux and spectrum of $\bar{\nu}_{\rm e}$ from power reactors has reached substantial sophistication. The first two "long baseline" experiments, Chooz and Palo Verde, have amply demonstrated the capability of this new breed of detectors, while providing solid evidence that $\nu_{\rm e} - \nu_{\mu}$ is *not* the dominant channel in the atmospheric neutrino oscillation. KamLAND, scheduled to begin data-taking in less than one year, will extend our reach for small mass-differences to unprecedented levels. Its size and background will move reactor-based experiments to a new dimension, with several new physics opportunities in the essentially background-less detection of $\bar{\nu}_{\rm e}$ from a number of natural sources. Direct observation of solar neutrinos is also among the future goals of this "ultimate" reactor experiment.

7 Acknowledgments

This review is rooted in the many daily discussions that accompanied the design, construction, data-taking and analysis of the Palo Verde experiment. Each one of the collaborators in a remarkably small and effective group contributed importantly to some of the results described here. They are Felix Boehm, Jerry Busenitz, Brian Cook, Herb Henrikson, Janos Kornis, David Lawrence, K.B. Lee, Kevin McKinny, Lester Miller, Vladimir Novikov, Andreas Piepke, Barry Ritchie, Dillon Tracy, Petr Vogel, Yi-Fang Wang and Joachim Wolf. I would also like to thank Junpei Shirai, Fumihiko Suekane and Atsuto Suzuki for bringing me up-to-speed quickly in many exciting early discussions on KamLAND. I am also indebted to Alessandro Baldini and Carlo Bemporad for interesting discussions on the Chooz data. Finally I would like to thank the organizers of the Summer Institute for the opportunity to present the subject and the flawless organization.

This work was supported in part by the US DoE grant DE-FG03-96ER40986.

References

[1] For early developments in neutrino physics see, for example, Chapter 1 in "Neutrino Physics", K. Winter, Ed., Cambridge University Press, 1991.

[2] G. Rameika, these Proceedings.

[3] For an up-to-date discussion of the neutrino masses and the relevant experiments see, for example P. Fisher, B. Kayser and K.S. McFarland, Ann. Rev. Nucl. Part. Sci. 49, 481 (1999) or K. Zuber, Physics Reports, 305 (1998) 296.

[4] See H. Murayama, these Proceedings, for an extensive discussion of the theoretical implications of finite neutrino masses.

[5] L. Wolfenstein, these Proceedings.

[6] D.E. Groom *et al.*, Europ. Phys. J. C15 (2000) 1.

[7] E. Kearns, these Proceedings.

[8] J. Wilkerson, these Proceedings.

[9] G. Feldman, these Proceedings.

[10] For a general discussion of short-baseline reactor experiments see F. Boehm and P. Vogel, Physics of Massive Neutrinos, Cambridge 1992.

[11] G. Zacek *et al.*, Phys. Rev. D34 (1986) 2621.

[12] B. Achkar *et al.*, Nucl. Phys. B434 (1995) 503.

[13] B. Achkar *et al.*, Phys. Lett. B374 (1996) 243.

[14] P.F. Harrison, D.H. Perkins and W.G. Scott, Phys. Lett. B349 (1996) 137.

[15] L. Mikaelyan, arXiv:hep-ex/0008046v2 25 Aug 2000, to appear in Proceeding of Neutrino 2000, Sudbury, Canada.

[16] L. Miller, PhD thesis, Stanford Sept 2000, unpublished.

[17] A.A. Hahn *et al.*, Phys. Lett. B218 (1989) 365.

[18] K. Schreckenbach *et al.*, Phys. Lett. B160 (1985) 325.

[19] Davis *et al.* Phys. Rev. C19 (1979) 2259;
P. Vogel *et al.* Phys. Rev. C24 (1981) 1543.

[20] H-V. Klapdor *et al.* Phys. Rev. Lett. 48 (1982) 127;
H-V. Klapdor *et al.* Phys. Lett. B112 (1982) 22.

[21] P. Vogel, Phys. Rev. D29 (1984) 1918.

[22] P. Vogel and J.F. Beacom, Phys. Rev. D60 (1999) 053003.

[23] M. Apollonio *et al.*, Phys. Lett. B420 (1998) 397.

[24] M. Apollonio *et al.*, Phys. Lett. B466 (1999) 415.

[25] F. Boehm *et al.*, Phys. Rev. Lett. 84 (2000) 3764.

[26] F. Boehm *et al.*, Phys. Rev. D62 (2000) 072002.

[27] A. Piepke *et al.*, Nucl. Instr. and Meth. A432 (1999) 392.

[28] A. Baldini *et al.*, Nucl. Instr. and Meth. A372 (1996) 207.

[29] G. Gratta *et al.*, Nucl. Instr. and Meth. A400 (1997) 456.

[30] Y-F. Wang *et al.*, Phys. Rev. D62 (2000) 013012.

[31] G.J. Feldman and R.D. Cousins, Phys. Rev. D57 (1998) 3873.

[32] Preliminary result, SuperKamiokande Collaboration; see K. Okamura, Ph.D. Thesis, University of Tokyo (1999).

[33] "US-Russian Plutonium Production Agreement is Signed", Statement by the White House office of the Vice President, 23 Sept. 1997.

[34] P. Alivisatos et al. "KamLAND: a liquid scintillator Anti-Neutrino Detector at the Kamioka site", Stanford-HEP-98-03, Tohoku-RCNS-98-15.

[35] G. Eders, Nucl. Phys. 78 (1966) 657.

[36] G. Marx, Czech. J. of Phys. B19 (1969) 1471;
G. Marx and I. Lux, Acta Phys. Acad. Hung. 28 (1970) 63;
C. Avilez *et al.*, Phys. Rev. D23 (1981) 1116.

[37] L. Krauss *et al.*, Nature 310 (1984) 191.

[38] R.S. Raghavan *et al.*, Phys. Rev. Lett. 80 (1998) 635.